ELECTRON CURRENT THROUGH THIN MICA FILMS

Thesis by

Malcolm Mc Coll

In Partial Fulfillment of the Requirements

For the Degree of

Doctor of Philosophy

California Institute of Technology

Pasadena, California

1964

(Submitted February 6, 1964)

ACKNOWLEDGEMENTS

I wish to express my sincere gratitude to my advisor, Professor C. A. Mead, for his stimulating encouragement and constructive suggestions during the preparation of this thesis. I am also grateful to Professor C. H. Wilts and to Dr. F. L. Vernon, Jr. of Aerospace Corporation for their helpful criticism of the manuscript.

I would like to acknowledge the financial support provided by means of fellowship grants from the Firestone Tire and Rubber Company, the General Electric Foundation, and the International Business Machines Corporation. This work was also supported in part by the Office of Naval Research and the International Telephone and Telegraph Company.

To my wife Sylvia special thanks are due for her patience, encouragement, and assistance throughout.

ABSTRACT

Muscovite mica, cleaving every 10Å, provides a crystalline insulator with uniformly parallel surfaces of well known separation ideally suited to the study of electron transport phenomena. Using a micro-splitting technique similar to that developed by Foote and Kazan, muscovite was cleaved in a vacuum of 10^{-6} Torr and metal electrodes evaporated, aluminum on one side, gold on the other. The current through 30 and 40Å films was measured as a function of voltage and temperature and analyzed in terms of the tunneling theory of Stratton. Using the actual image-force barrier shape, the approximately symmetrical volt-ampere data gave barrier heights of $\varphi_o = 0.95$ and 0.93eV for the 40 and 30Å films, respectively, for an effective mass ratio of $m^*/m = 0.92$. The theoretical temperature dependence was observed in the 40Å film from room temperature down to liquid nitrogen temperature (77^oK). Thicker films 50 to 10,000Å, exhibited temperature dependent volt-ampere curves linear in log I versus $\sqrt{V}$ over a factor of 10:1 in voltage and a thermal activation energy of 0.55eV, lower than he barrier height above possibly because of injection into polaron states. Preliminary photoelectric response data yielded $\varphi_o = 0.8$eV, raising some question as to the real meaning of the φ_o found from tunneling theory.

TABLE OF CONTENTS

INTRODUCTION

The mechanism of electrons tunneling through insulating films has received considerable attention in the last few years as a result of both the device possibilities utilizing tunneling[1] and also the success of tunneling in the study of superconductivity.[2] Until the recent paper by Hartman[3] using aluminum oxide, there has been no reported successful quantitative experimental fit to the theory. Even in this case, however, much is left to be desired. The method of fabrication resulted in a polycrystalline insulator, the stoichiometry of which is non-uniform from one side to the other. This would produce a non-uniform dielectric constant which could mean the actual barrier shape is much different from that calculated from image forces. Different barrier heights were measured at each interface of the Al-Al_2O_3-Al diode, although not necessarily as a result of the non-uniform dielectric constant itself.

Muscovite mica being split as a thin film from a bulk sample not only overcomes these disadvantages but also provides an insulating thin film whose physical properties such as its dielectric constant, trapping levels and their density, forbidden energy gap, etc. are identical to the easily measurable bulk values. Furthermore, it is a single crystal insulator whose cleavage planes 10Å apart[4] (see Fig. 1) provide uniformly parallel surfaces of well known separation ideally suited to the study of electron transport phenomena.

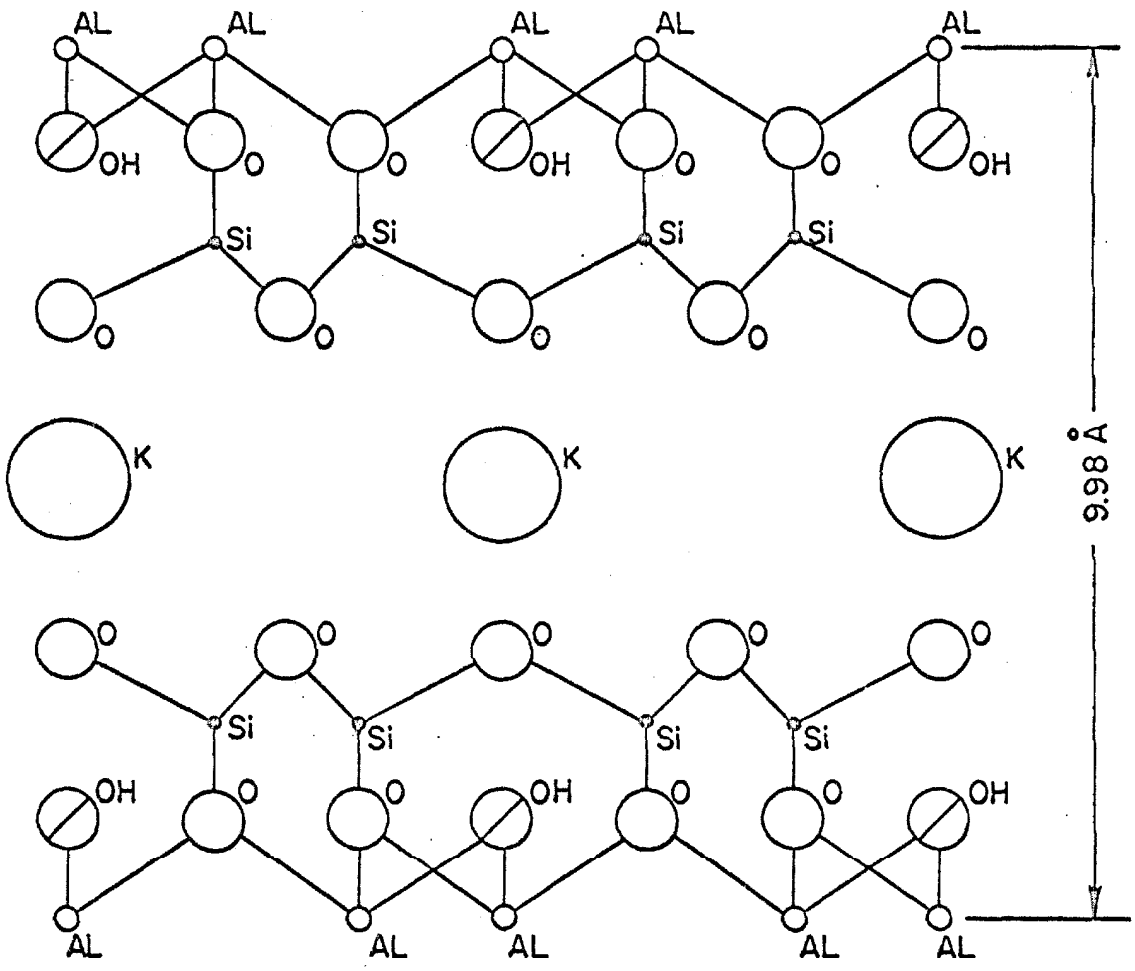

Fig. 1. Crystal structure of muscovite (after Hückel[4]). Cleavage occurs in the potassium plane. [4]For a more comprehensive configuration see Norton.

Von Hippel[5] using a 6.5μ thick sample was the first to observe the high field conductivity ($\approx 5 \times 10^6$ V/cm) of mica. No attempt at an empirical formula was made, but Von Hippel felt from intuitive arguments that the current was being space-charge limited by trapped electrons. Maltsea[6] has made a more recent investigation at high fields and observed a dependence of the conductivity σ on the field F of the form $\sigma = \sigma_o \exp \beta\sqrt{F}$. This dependence was attributed to the Frenkel effect,[7] a Schottky type of emission from filled traps. No mention in the English abstract was made of the thicknesses of his samples nor, and more importantly, of how well the value of β fits Frenkel's theory. In 1962 Foote and Kazan[8] developed a technique for splitting mica down to less than 100Å and observed a dependence of the current density J on the field of the form $J = J_o \exp \beta\sqrt{F}$ on a thin sample thought to be 40Å thick. Assuming that this was a Schottky emission process and that the appropriate dielectric constant for such a mechanism would be closer to a low frequency value of 7.6, they calculated from β an independent thickness of the mica of 36Å. No further investigation was made of the phenomenon. However, the work being reported in this thesis would indicate that the film measured by Foote and Kazan was probably 60Å thick, the error arising from the measurement of the very small metal-insulator-metal diode areas that were used along with the diode capacitance and dielectric constant to calculate the thickness.

In the research reported in this thesis Foote and Kazan's technique was modified to cleave muscovite in a vacuum of 10^{-6} Torr, after which metal electrodes were evaporated creating Au-mica-Al diodes. The aluminum was chosen because of its strong adhesion to mica, as necessitated by the cleaving process, and the gold because contact could be made easily mechanically. The volt-ampere and temperature characteristics of the 30 and 40Å films were successfully analyzed in terms of Stratton's[9] tunneling theory for voltages less than 0.5 volts using a new and very accurate approximation to the image-force barrier shape. For voltages greater than the metal-insulator work function, the theory breaks down completely, but the data provide insight into the nature of the conduction band in muscovite. Temperature dependence for thicker films is discussed in terms of polaron injection. And finally, the preliminary photoelectric data suggest that further theoretical considerations must be included in the theory on tunneling.

CHAPTER I

THEORY

1.1 Emission Into a Thick Insulator

The mechanisms of thermionic and cold emission of electrons from a metal surface into a vacuum are well understood and have been analyzed from a general viewpoint by Murphy and Good.[10] For the experiments performed in this thesis one needs a solution to the similar situation where the vacuum is replaced by an insulator of dielectric constant K and an effective mass m^*, which the electron exhibits while traveling through the insulator. The treatment below parallels that found in Murphy and Good.

The free-electron theory of metals gives the following for the supply function or the number of electrons per second per cm^2 incident on the barrier whose x-directed component of energy, W, lies within dW

$$N(T, \zeta, W)dW = \frac{4\pi mkT}{h^3} \ln\left[1 + \exp\left(-\frac{W - \zeta}{kT}\right)\right] dW \qquad (1)$$

where m, k, T, h and ζ are the electron mass, Boltzmann's constant, absolute temperature, Planck's constant and the energy of the Fermi level respectively. As shown in Fig. 2, all energies will be referred to the bottom of the conduction band far inside the insulator with no applied field. Then the work function φ_o becomes $-\zeta$. In addition the energy W is the sum of the kinetic and potential energies

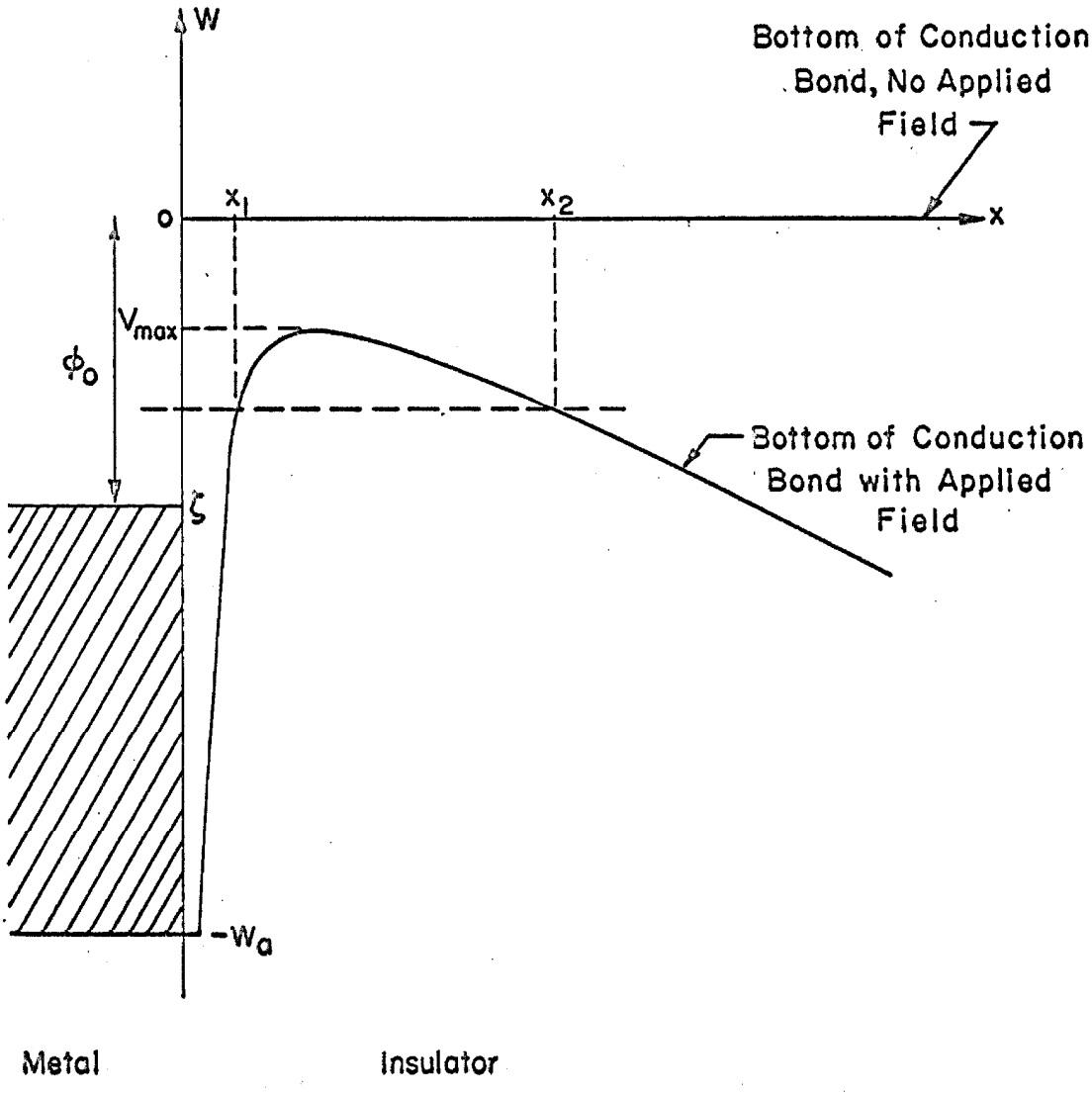

Fig. 2. Potential energy diagram of an electron in an insulator near a metal surface.

$$W = \frac{p^2(x)}{2m^*} + V(x) \tag{2}$$

where m^* is the effective mass in the insulator. Assuming the image field and applied field F in the insulator of dielectric constant K effectively account for the forces on an electron in the insulator

$$V(x) = -\frac{e^2}{4Kx} - eFx \qquad \text{for } x > 0 \tag{3}$$

and

$$V(x) = -W_a \qquad \text{for } x < 0 \tag{4}$$

where $-W_a$ is the effective constant potential energy inside the metal. Near the metal-insulator interface $V(x)$ is assumed to connect smoothly with the functions in equations 3 and 4 as shown in Fig. 2.

Murphy and Good found that

$$D(F, W) = \left[1 + \exp\left(-\frac{2i}{\hbar}\int_{x_1}^{x_2} p(\xi)\, d\xi\right)\right]^{-1} \tag{5}$$

is a good approximation for the probability, $D(F, W)$, that an incident electron is transmitted into the conduction band of the insulator. As illustrated in Fig. 2, x_1 and x_2 are the classical turning points for an energy W. From equations 2 and 3

$$p(x) = \left[2m^*\left(W + \frac{e^2}{4Kx} + eFx\right)\right]^{1/2} \tag{6}$$

from which

$$x_1 = (-W/2eF)\left[1 + (1 - \frac{e^3F}{KW^2})\right]^{1/2} \quad (7)$$

$$x_2 = (-W/2eF)\left[1 - (1 - \frac{e^3F}{KW^2})\right]^{1/2} \quad (8)$$

The exponent in equation 5 may be rewritten

$$-2i\hbar^{-1}\int_{x_1}^{x_2} p(\xi)d\xi = \frac{4\sqrt{2}}{3}\left[\frac{FK^3\hbar^4}{(m^*)^2 e^5}\right]^{-1/4} y^{-3/2}v(y) \quad (9)$$

where

$$y = \frac{(e^3F/K)^{1/2}}{|W|} \quad (10)$$

$$v(y) = -\frac{3i}{4\sqrt{2}}\int_{1-(1-y^2)^{1/2}}^{1+(1-y^2)^{1/2}} (\rho - 2 + y^2\rho^{-1})^{1/2}d\rho \quad (11)$$

or

$$v(y) = 2^{-1/2}(1+a)^{1/2}\left\{\hat{E}\left[\frac{(2a)^{1/2}}{(1+a)^{1/2}}\right] - (1-a)\hat{K}\left[\frac{(2a)^{1/2}}{(1+a)^{1/2}}\right]\right\} \quad (12)$$

where

$$a = (1-y^2)^{1/2} \quad (13)$$

and $\hat{K}$ and $\hat{E}$ are complete elliptic integrals of the first and second kind respectively.

Substituting equation 9 into 5

$$D(F, W) = \left\{1 + \exp\left[\frac{4\sqrt{2}}{3}\left(\frac{FK^3\hbar^4}{(m^*)^2 e^5}\right)^{-1/4} y^{-3/2} v(y)\right]\right\} \tag{14}$$

One might expect this equation to have no meaning for values of W greater than $W = V_{max} = -(e^3F/K)^{1/2}$ because x_1 and x_2 then become complex numbers. However Murphy and Good explain that even though the validity of equation 14 does in fact deteriorate above this point, it turns out that the current contribution at these energies is unimportant.

Hence the total electric current density is found from equations 1 and 14.

$$j(F, T, \zeta) = e\int_{-W_a}^{\infty} D(F, W)N(T, \zeta, W)dW \tag{15}$$

$$= \frac{4\pi mkTe}{h^3}\int_{-W_a}^{\infty} \frac{\ln\{1+\exp[-(W-\zeta)/kT]\}\,dW}{1+\exp\frac{4\sqrt{2}}{3}\left(\frac{FK^3\hbar^4}{(m^*)^2e^5}\right)^{-1/4} y^{-3/2}v(y)}$$

At this point it is convenient to introduce Hartree units defined in Table I.

Table I

One Hartree unit of	Equivalent to
current density j	$m^3 e^9 \hbar^{-7}$ or 2.37×10^{14} A/cm^2
electric field F	$m^2 e^5 \hbar^{-4}$ or 5.15×10^9 V/cm
energy ζ, kT, W	$m\, e^4 \hbar^{-2}$ or 27.2 eV

In these new units equation 15 becomes,

$$j(F,\ T,\ \zeta) = \frac{kT}{2\pi^2} \int_{-W_a}^{\infty} \frac{\ln \{1 + \exp [-(W - \zeta)/kT]\}\ dW}{1 + \exp \frac{4\sqrt{2}}{3} m_r^{1/2} (K^3 F)^{-1/4} y^{-3/2} v(y)} \tag{16}$$

where

$$m_r = \frac{m^*}{m} \tag{17}$$

Equation 16 is now approximated in closed form by means of three separate approximations to the integrand which lead to three dis-

tinct regions of operation: thermionic emission, field emission, and a narrow intermediate region between the two.

1.1a Thermionic Emission

The approximations used here are valid under the conditions that the peak in the current density integrand in equation 16 occurs when W lies close to V_{max}, and its low energy tail has fallen off appreciably for energies a few kT above the Fermi level. Under these conditions one may expand v(y) around $W = V_{max} = -(F/K)^{1/2}$

$$\frac{4\sqrt{2}}{3} m_r^{1/2} (K^3F)^{-1/4} y^{-3/2} v(y) = -\pi m_r^{1/2} (K^3F)^{-1/4} \epsilon + \frac{3}{16} \pi m_r^{1/2} (K^3F)^{-1/4} \epsilon + \ldots \tag{18}$$

where

$$\epsilon = 1 + W\left(\frac{F}{K}\right)^{-1/2} = (y-1)/y \tag{19}$$

and

$$\ln\left[1 + \exp\left(-\frac{W-\zeta}{kT}\right)\right] = \exp\left(-\frac{W-\zeta}{kT}\right) - \frac{1}{2}\exp\left[-2\frac{W-\zeta}{kT}\right] + \ldots. \tag{20}$$

Taking only the first term in each expansion one arrives at

$$j = \frac{kT}{2\pi^2} \int_{-W_a}^{\infty} \frac{\exp\left[-(W-\zeta)/kT\right]dW}{1+\exp\left\{-\pi m_r^{1/2}(K^3F)^{-1/4}\left[1+W(F/K)^{-1/2}\right]\right\}} \quad (21)$$

from equation 16. Clearly $-W_a$ may be replaced by $-\infty$ and this integration leads to

$$j = \frac{(kT)^2}{2\pi^2} \frac{\pi g}{\sin \pi g} \exp\left[-\frac{\varphi_o - \left(\frac{F}{K}\right)^{1/2}}{kT}\right] \quad (22)$$

where

$$g = \frac{K^{1/4}F^{3/4}}{\pi m_r^{1/2} kT} \quad (23)$$

The conditions that equation 22 be a valid approximation are

$$\ln\left(\frac{1-g}{g}\right) - \frac{1}{g(1-g)} > -\pi m_r^{1/2} K^{-1/4} F^{-3/4}\left[\varphi_o - (F/K)^{1/2}\right] \quad (24)$$

and

$$\ln\left(\frac{1-g}{g}\right) - \frac{1}{1-g} > -\pi m_r^{1/4}(K^3F)^{-1/8} \quad (25)$$

Restrictions 24 and 25 are a result of the first term approximations of 20 and 18 respectively and include the necessary condition that g must be less than unity, i.e., low fields or high temperatures.

Note that equation 22 differs from the well known Schottky equation only by the factor $\pi g/\sin\pi g$, which approaches unity for small g.

1.1b Field Emission

The requirement for field emission is essentially that the peak in the current density integrand be centered around the Fermi level and that its tail for higher energy electrons has fallen off appreciably at $W = V_{max}$. In the approximation of equation 16 used here the exponent in the denominator is much larger than unity, i.e.,

$$\left[1 + \exp \frac{4\sqrt{2}}{3} m_r^{1/2} (K^3F)^{-1/4} y^{-3/2} v(y)\right]^{-1} \approx \exp - \frac{4\sqrt{2}}{3} m_r^{1/2} (K^3F)^{-1/4} y^{-3/2} v(y) \tag{26}$$

and the latter argument in turn is expanded about the Fermi level, retaining only the first two terms:

$$-\frac{4\sqrt{2}}{3} m_r^{1/2}(K^3F)^{-1/4} y^{-3/2} v(y) = -b + c(W - \zeta) - f(W - \zeta)^2 + \ldots \quad (27)$$

where

$$b = \frac{4}{3}\sqrt{2}\, m_r^{1/2} F^{-1} \varphi_o^{3/2} V\left(\frac{(F/K)^{1/2}}{\varphi_o}\right) \quad (28)$$

$$c = 2\sqrt{2}\, m_r^{1/2} F^{-1} \varphi_o^{1/2} t\left(\frac{(F/K)^{1/2}}{\varphi_o}\right) \quad (29)$$

$$f = \frac{\sqrt{2}}{2} m_r^{1/2} F^{-1} \varphi_o^{3/2} (\varphi_o^2 - F/K)^{-1} v\left(\frac{(F/K)^{1/2}}{\varphi_o}\right) \quad (30)$$

and where

$$t(y) = v(y) - \frac{2}{3} y \frac{dv(y)}{dy} \quad (31)$$

Making these substitutions into equation 16

$$j = \frac{kT}{2\pi} \int_{-W_a}^{\infty} \exp\left[-b + c(W-\zeta)\right] \ln\left\{1 + \exp\left[-(W-\zeta)/kT\right]\right\} dW \quad (32)$$

Again replacing $-W_a$ by $-\infty$ and integrating,

$$j = \frac{F^2}{16 m_r \pi^2 \varphi_o t^2} \left(\frac{\pi c k T}{\sin \pi c k T}\right) \exp\left(-\frac{4\sqrt{2}\, m_r^{1/2} \varphi_o^{3/2} v}{3F}\right) \quad (33)$$

The restrictions this time being

$$\varphi_o - (F/K)^{1/2} > \pi^{-1} m_r^{1/2} K^{1/4} F^{3/4} + kT(1 - ckT)^{-1} \tag{34}$$

$$1 - ckT > (2f)^{1/2}\, kT \tag{35}$$

The arguments of v and t are $\frac{(F/K)^{1/2}}{\varphi_o}$. Equation 34 places a maximum on the field and states that equation 33 is no longer valid when V_{max} approaches the Fermi level. The validity of the two term expansion is contained in equation 35, a restriction appropriate for low fields which in turn means that $ckT < 1$.

Equation 33 differs from the temperature independent Fowler-Nordheim [11] formula by the factor $\pi ckT/\sin(\pi ckT)$, which again approaches unity for small ckT. Equation 33 becomes somewhat more tractable if one introduces the approximations:

$$v(y) \approx 1 - y^2 = 1 - \frac{F/K}{\varphi_o^2} \tag{36}$$

$$t(y) \approx 1 \tag{37}$$

which are good to about 10% for the fields usually encountered.

1.1c Intermediate Region

A solution to the region in between the above can be obtained by use of the first term approximations of equations 20 and 26.

Equation 16 then becomes

$$j = \frac{kT}{2\pi^2} \int_{-W_a}^{\infty} \exp\left[- \frac{W - \zeta}{kT} - \frac{4/2\, m_r^{1/4} v(y)}{3(K^3 F)^{1/2} y^{3/2}} \right] dW \qquad (38)$$

In this region the integrand of equation 38 must be appreciable only for energies which lie between the Fermi energy and V_{max}. Expanding the second term in the exponent to three terms around the energy η, at which the integrand is at its maximum value, and evaluating it by means of the saddle point method, the current density becomes

$$j = \frac{F}{2\pi} \left(\frac{kTt}{2\pi m_r} \right)^{1/2} \exp\left[- \frac{\varphi}{kT} + \frac{F^2 \omega}{24 m_r (kT)^3} \right] \qquad (39)$$

where

$$\omega = 3t^{-2} - 2vt^{-3} \qquad (40)$$

$$\eta = \frac{-F^2}{8 m_r (kT)^2 t^2} \qquad (41)$$

and the arguments of v and t are $\frac{(F/K)}{-\eta}$

The conditions for equation 39 to be a good solution are

$$\frac{-\eta}{(F/K)^{1/2}} > 1 + \eta^{-1}\, m_r^{-1/2} K^{3/4} F^{1/4} \frac{g}{g-1} \qquad (42)$$

and

$$\frac{-F^2}{8m_r(kT)^2 t_\eta} > -\varphi_o + kT \frac{1}{1-F(2\sqrt{2}\, m_r^{1/2} \varphi_o^{1/2} kT t_\varphi)^{-1}} \qquad (43)$$

where $t_\varphi = t\left(\frac{(F/K)^{1/2}}{\varphi_o}\right)$ and $t_\eta = t\left(\frac{(F/K)^{1/2}}{-\eta}\right)$. The first condition comes from considering only the first term approximation of equation 20 and is concerned with energies near the Fermi level.

As an example of the fields required at room temperature for these regions to be obtained, Table II illustrates the case for $\varphi_o = 1$ eV, $m_r = 1$ and $K = 2.5$.

Table II

F V/cm	Region
5×10^5	Thermionic
1.0×10^6	Thermionic
1.5×10^6	
2.0×10^6	Intermediate
2.5×10^6	Intermediate
3.0×10^6	
3.5×10^6	Field
4.0×10^6	Field
4.5×10^6	Field
5.0×10^6	Field

1.2 Tunneling Through Thin Insulating Films

For a thin insulator sandwiched between two identical metal electrodes the effect of the additional electrode is to change both the supply function and the potential barrier. Figure 3 illustrates the geometry of the situation where V is the voltage applied across the diode.

Harrison[13] showed the effect of the second electrode on the supply function (given in equation 1 for one electrode only) was essentially to include a reverse current whose supply function was identical to the first except the Fermi level of the second is eV less

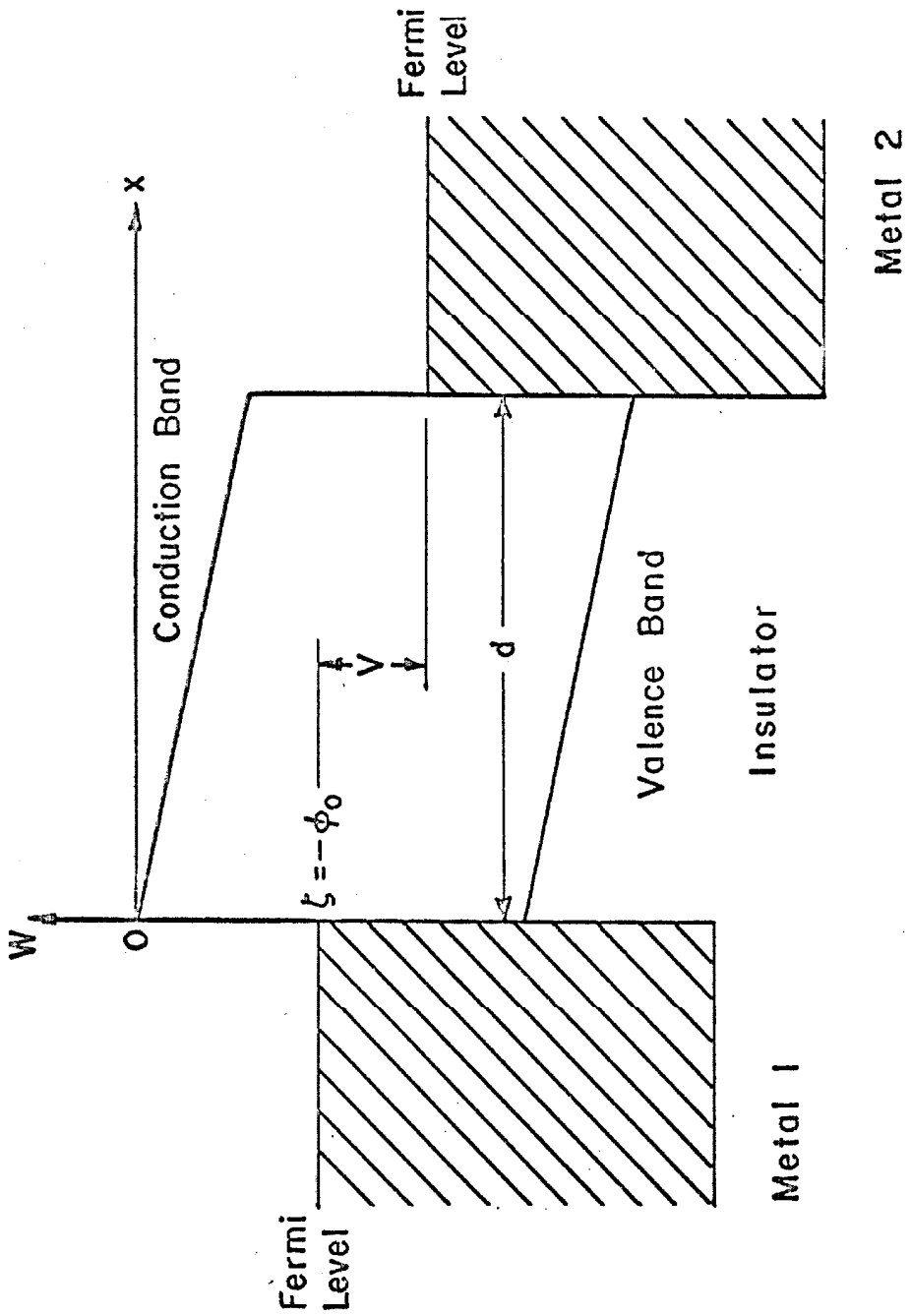

Fig. 3. Energy diagram of an electron for a symmetrical metal-insulator-metal diode excluding the image-force potential.

than for the first electrode:

$$N(T,\ \zeta,\ W)\ dW = \frac{4\pi mkT}{h^3}\ \ln\left\{\frac{1+\exp\left[-(w-\zeta)/kT\right]}{1+\exp\left[-(w-\zeta+eV)/kT\right]}\right\} dW \quad (44)$$

in cgs units for a symmetrical function.

Stratton[9] used an approach to this problem very similar to that used by Murphy and Good.[10] (See preceding chapter.)

$$\ln D(F,\ W) = -\frac{2}{\hbar}\ (2m^*) \int_{x_1}^{x_2} \sqrt{\varphi(x) - W}\ dx \quad (45)$$

Here $\varphi(x)$ represents not only the potential of the applied field and the first image of the electron in metal but $\varphi_i(x)$, the sum of the potentials of the image charges necessary to establish the electrode planes as equipotentials:

$$\varphi(x) = \varphi_i(x) - e\ \frac{V}{d}\ x \quad (46)$$

Expanding equation 45 around the Fermi level

$$\ln D(F,\ W) = -\left(b_1 + c_1\epsilon_x + f_1\epsilon_x^{\ 2} + \ldots\right) \quad (47)$$

where

$$\epsilon_x = W-\zeta \quad (48)$$

and the subscript 1 refers to metal 1. From equations 45, 47

and 48 it follows

$$b_1 = \alpha \int_{x_1}^{x_2} [\varphi(x) - \zeta]^{1/2}\, dx \tag{49}$$

$$c_1 = \alpha \int_{x_1}^{x_2} [\varphi(x) - \zeta]^{-1/2}\, dx \tag{50}$$

$$f_1 = \frac{\alpha}{4}\left\{\frac{1}{x_2 - x_1}\left[\frac{1}{\varphi'(x_1)} - \frac{1}{\varphi'(x_2)}\right]\int_{x_1}^{x_2} \frac{dx}{[\varphi(x) - \zeta]^{1/2}}\right.$$

$$\left. - \frac{1}{2}\int_{x_1}^{x_2} \frac{dx}{[\varphi(x)-\zeta]^{3/2}}\left[1 - \frac{\varphi'(x)}{x_2-x_1}\left(\frac{x-x_1}{\varphi'(x_2)} + \frac{x_2-x}{\varphi'(x_1)}\right)\right]\right\} \tag{51}$$

where

$$\alpha = \frac{2(2m^*)^{1/2}}{\hbar} = 1.025\left(\frac{m^*}{m}\right)^{1/2} \text{ eV}^{-1/2}\text{Å}^{-1} \tag{52}$$

Keeping only the first two terms in equation 47, equations 44, 47, and 15 yield

$$j = \frac{A\exp(-b_1)}{(c_1 kT)^2}\,\frac{\pi c_1 kT}{\sin(\pi c_1 kT)}\,[1 - \exp(-c_1 V)] \tag{53}$$

where $A = 4\pi me(kT)^2/h^3 = 120T^2 Acm^{-2}$. This is identical in form to equation 33 except for the inclusion of the reverse current arising from the inclusion of the supply function of the second electrode. Now, however, b and c are given by equations 49 and 50. The restrictions on equation 53 are

$$1 - c_1 kT > kT(2f_1)^{1/2} \tag{54}$$

$$\varphi_m - \zeta - kT(1-c_1 kT)^{-1} > 0, \quad D(\Omega) = e^{-1} \tag{55}$$

where φ_m is the maximum value of $\varphi(x)$.

Stratton now expands b_1 and c_1 in powers of V;

$$b_1 = b_{10} - b_{11}V + b_{12}V^2 + \ldots \tag{56}$$

$$c_1 = c_{10} - c_{11}V + c_{12}V^2 + \ldots \tag{57}$$

and to terms of the order of V^2 in b_1

$$j = j_{10} \frac{\pi c_{10} kT}{\sin(\pi c_{10} kT)} [\exp(b_{11}V - b_{12}V^2)][1 - \exp(-c_{10}V)] \tag{58}$$

where

$$j_{10} = A(c_{10}kT)^{-2} \exp(-b_{10}) \tag{59}$$

For a symmetrical diode, however as shown by Stratton

$$b_{11} = \frac{1}{2} c_{10} \tag{60}$$

and

$$j = G(T) \left[V + V^3 \left(\frac{1}{24} c_{10}^2 - b_{12} \right) + \ldots \right] \tag{61}$$

where

$$G(T) = j_{10} c_{10} \frac{\pi c_{10} kT}{\sin \pi c_{10} kT} \tag{62}$$

The last two are the desired equations for making experimental parameter adjustments at low voltages.

Sommerfeld and Bethe[13] have shown the image force correction is

$$\varphi_i(x) = \frac{q^2}{4Kd} \left[\psi\left(- \frac{x}{d} \right) + \psi\left(\frac{x}{d} - 1 \right) - 2\psi(0) \right] \tag{63}$$

where

$$q^2 = 14.4 \text{ eV}\mathring{A} \tag{64}$$

and

$$\psi(z) = \frac{d\ln(z!)}{dz} \tag{65}$$

is Gauss's psi function and is tabulated in Jahnke and Emde.[14] Figure 4 shows $\varphi_i(x)$ plotted along with the approximate functions

$$\varphi_i(x) = -\frac{q^2}{4Kx}\ ; \qquad 0 \le \frac{x}{d} \le 1/4 \tag{66}$$

$$\varphi_i(x) = \frac{-q^2}{4Kd}\left[4\ln 2 + 20\left(\frac{1}{2} - \frac{x}{d}\right)^2\right]; \qquad \frac{1}{4} \le \frac{x}{d} \le 1/2 \tag{67}$$

These approximations, which have not appeared in the literature before, fit the actual image potential exactly at the extremes $x/d = 0$ and $1/2$ and are only in error 4% at $x/d = 1/4$. From these, b_{10} and c_{10} can be expressed analytically as

$$b_{10} = 2\alpha d\left(\frac{q^2}{4Kd}\right)^{1/2}\left\{\frac{(\Phi - 4)^{1/2}}{4} - \frac{1}{\Phi^{1/2}}\ln\left[\frac{\Phi^{1/2} + (\Phi^{1/2}-4)^{1/2}}{2}\right]\right\}$$

$$+ \alpha d\left(\frac{5q^2}{Kd}\right)^{1/2}\left[\frac{(\Phi_1 - .0625)^{1/2}}{4} + \Phi_1 \sin^{-1}\left(\frac{1}{4\Phi_1^{1/2}}\right)\right] \tag{68}$$

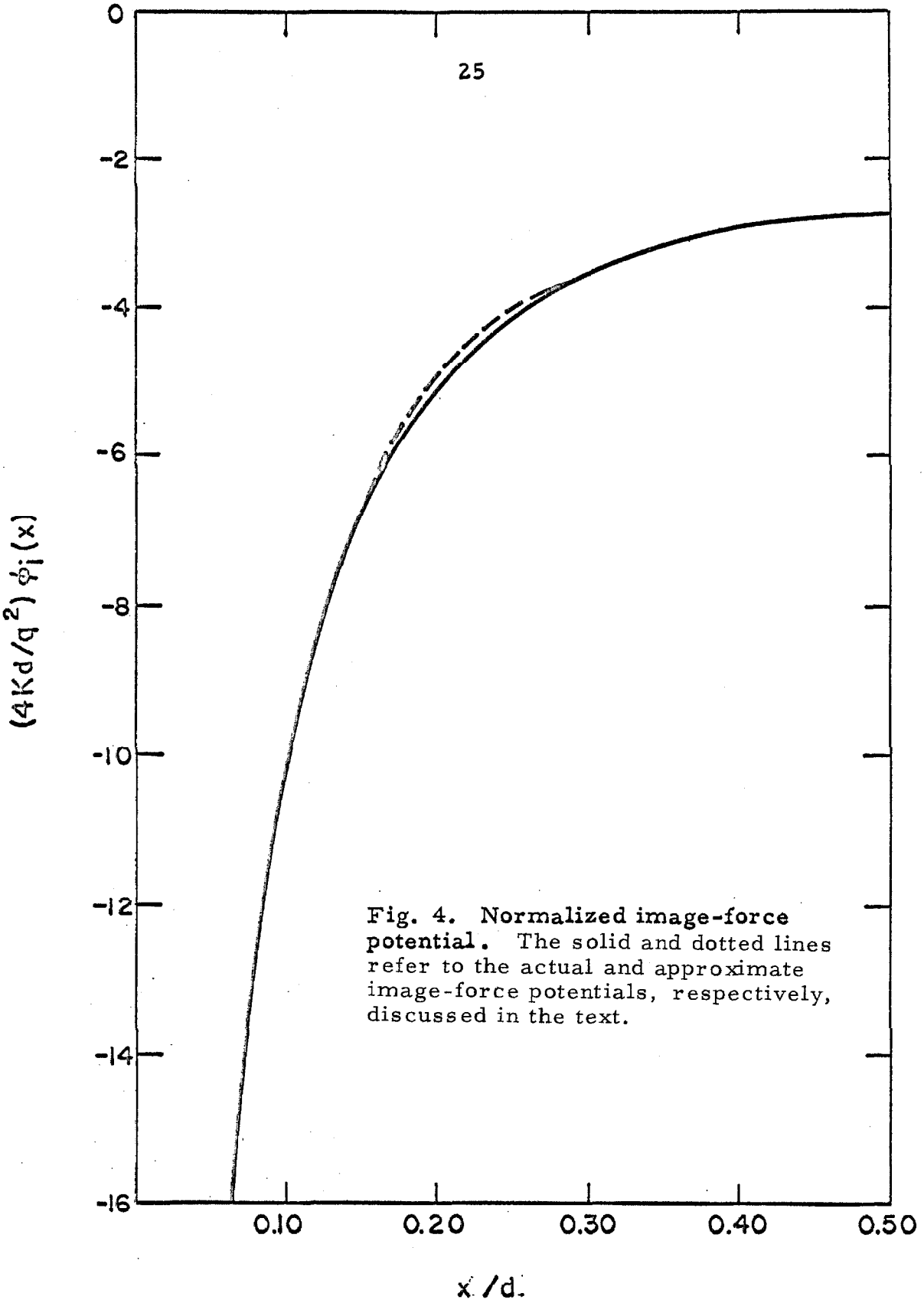

Fig. 4. Normalized image-force potential. The solid and dotted lines refer to the actual and approximate image-force potentials, respectively, discussed in the text.

$$c_{10} = \frac{\alpha d}{\Phi_o} \left(\frac{q^2}{4Kd}\right)^{1/2} \left\{ \frac{(\Phi - 4)^{1/2}}{4} + \frac{1}{\Phi^{1/2}} \ln\left[\frac{\Phi^{1/2} + (\Phi - 4)^{1/2}}{2} \right] \right\} \tag{69}$$

$$+\alpha d \left(\frac{Kd}{5q^2} \right)^{1/2} \sin^{-1} \left(\frac{1}{4\Phi_1^{1/2}} \right)$$

where

$$\Phi = \frac{4Kd}{q^2} \varphi_o \tag{70}$$

$$\Phi_1 = \frac{Kd}{5q^2} \varphi_o - \frac{\ln 2}{5} \tag{71}$$

and φ_o is the work function. Figure 5 is a plot of b_{10}, c_{10}, and b_{10}/c_{10} as a function of φ_o for $K = 2.5$. These values should be accurate to better than 1%.

1.3 Ionic Crystals and the Polaron

The energy band scheme for crystals is a result of the interaction between the electron and the electrostatic field of a perfectly rigid crystal lattice. If the crystal is ionic, however, the polarization displacement of the ions surrounding the electron's coulomb field produces a potential well which must be considered. This description of an electron moving in a potential produced by the induced ionic polarization is called a polaron. This section will in-

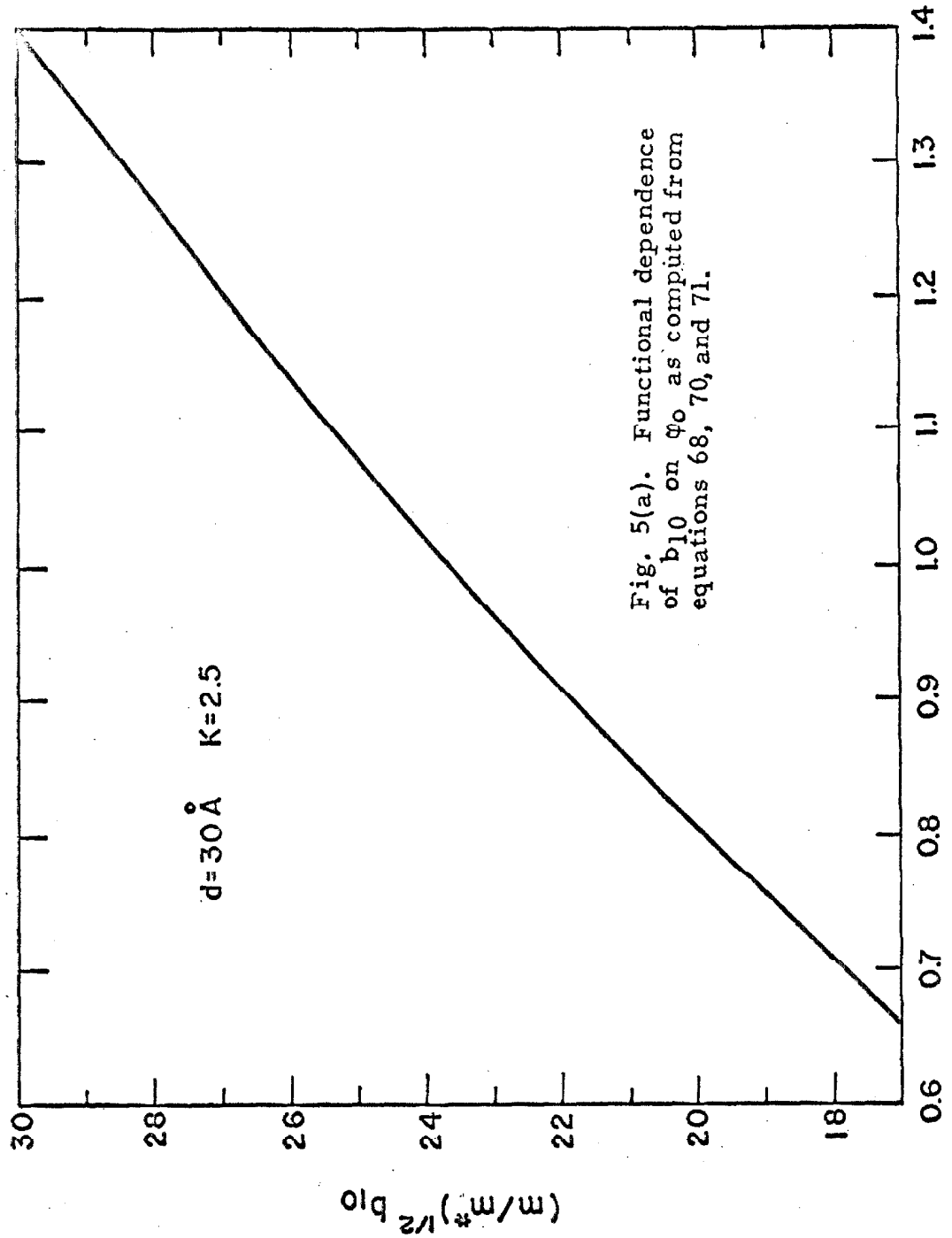

Fig. 5(a). Functional dependence of b_{10} on φ_o as computed from equations 68, 70, and 71.

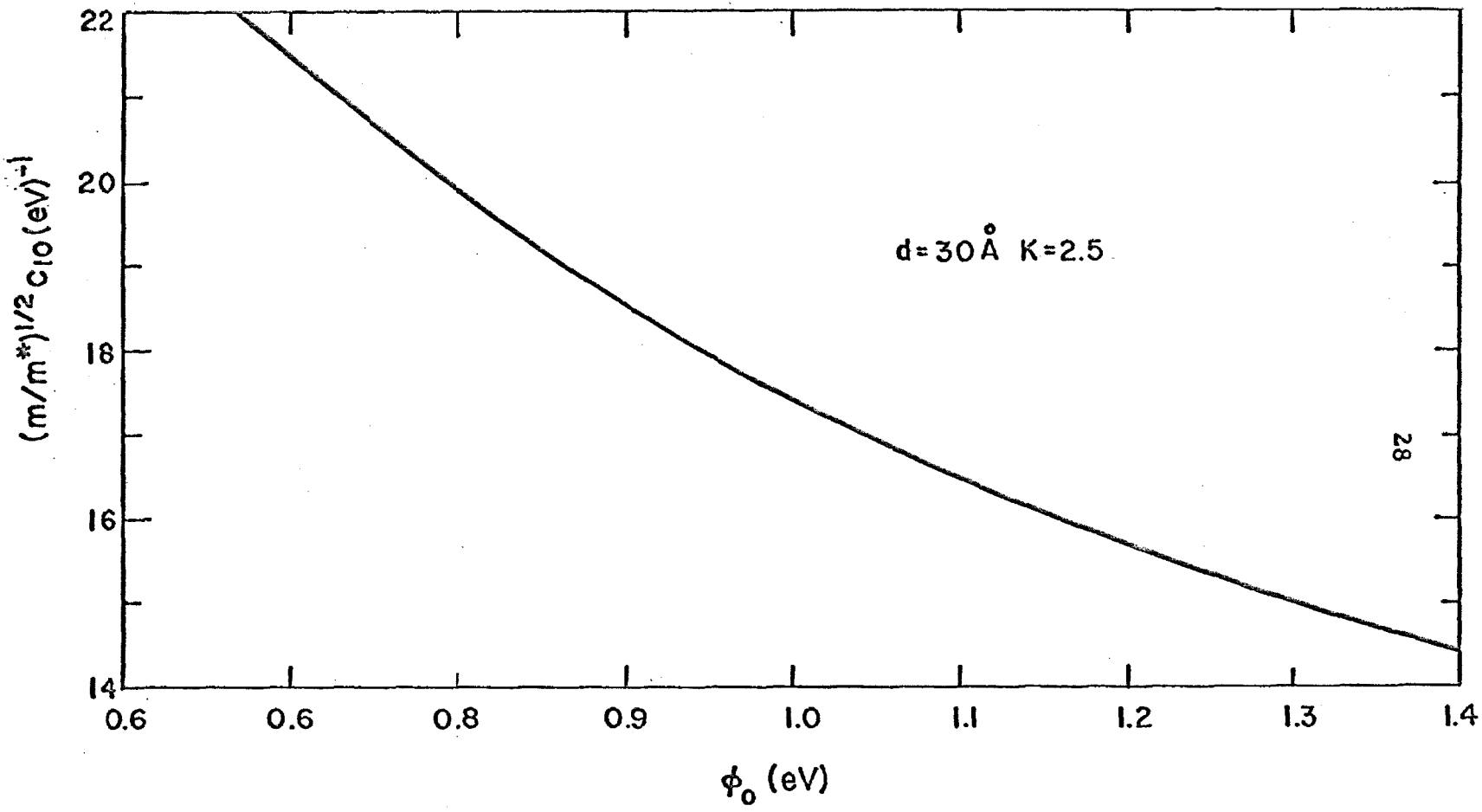

Fig. 5(b). Functional dependence of c_{10} on φ_o as computed from equations 69, 70, and 71.

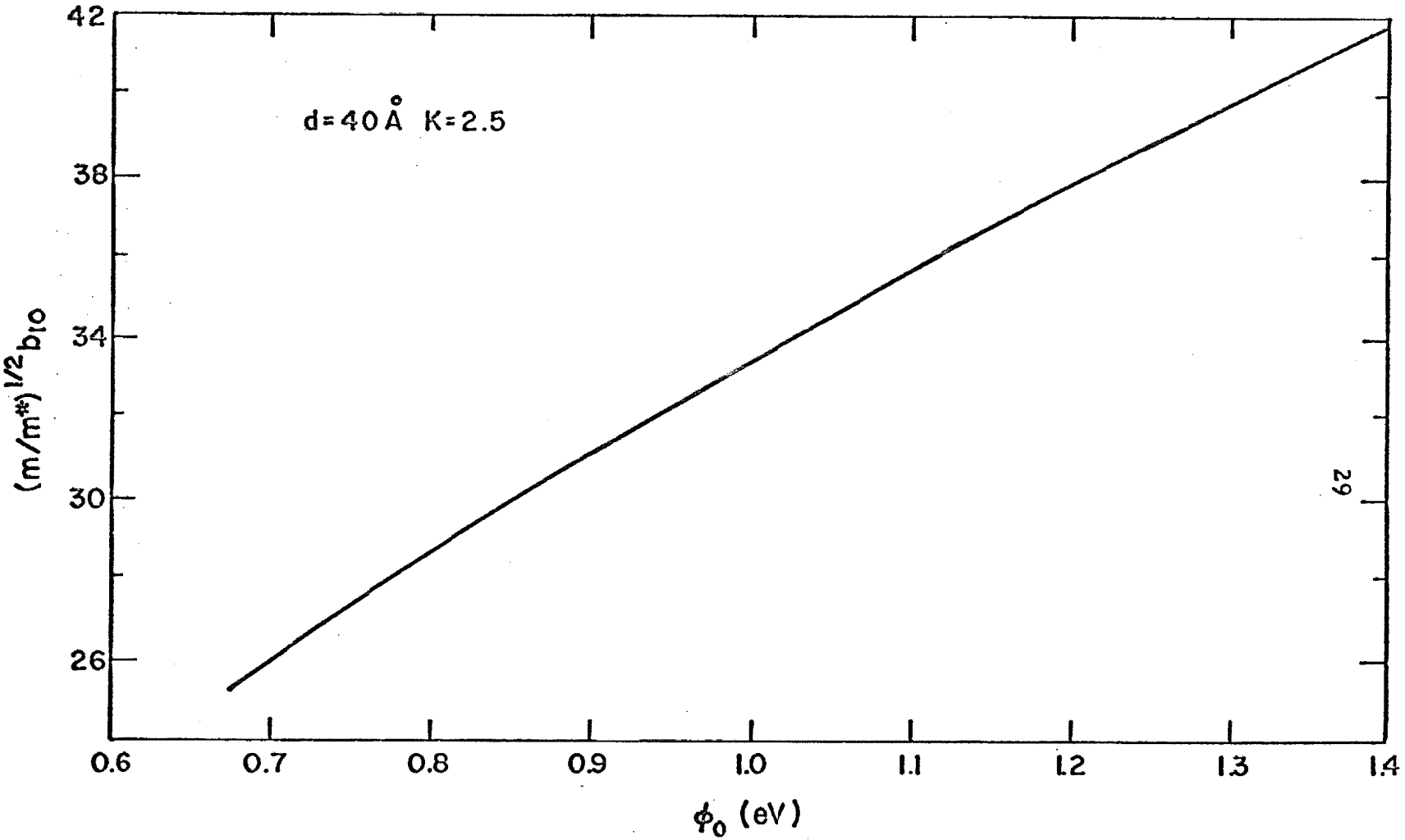

Fig. 5(c). Functional dependence of b_{10} on φ_o as computed from equations 68, 70, and 71.

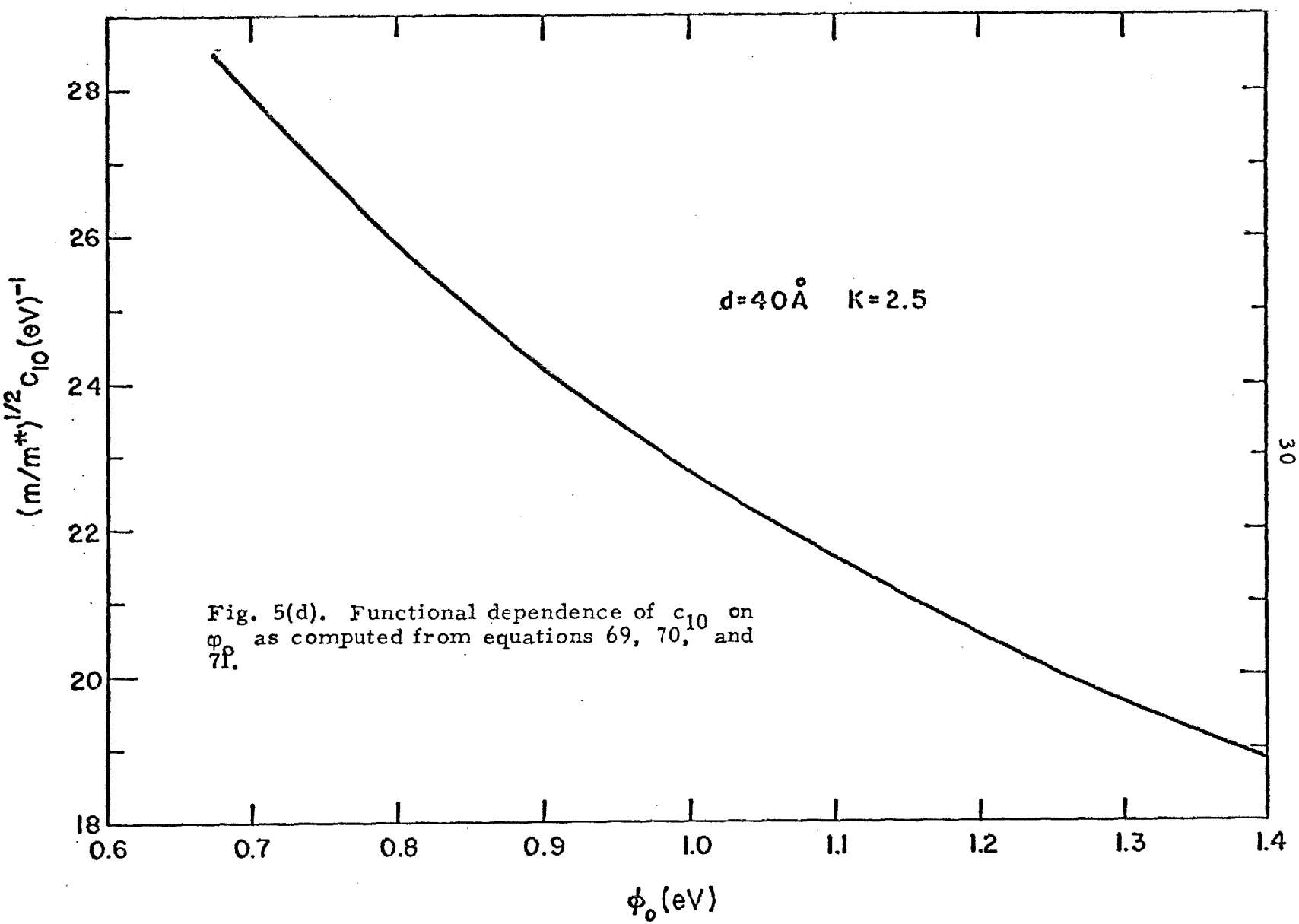

Fig. 5(d). Functional dependence of c_{10} on φ_0 as computed from equations 69, 70, and 71.

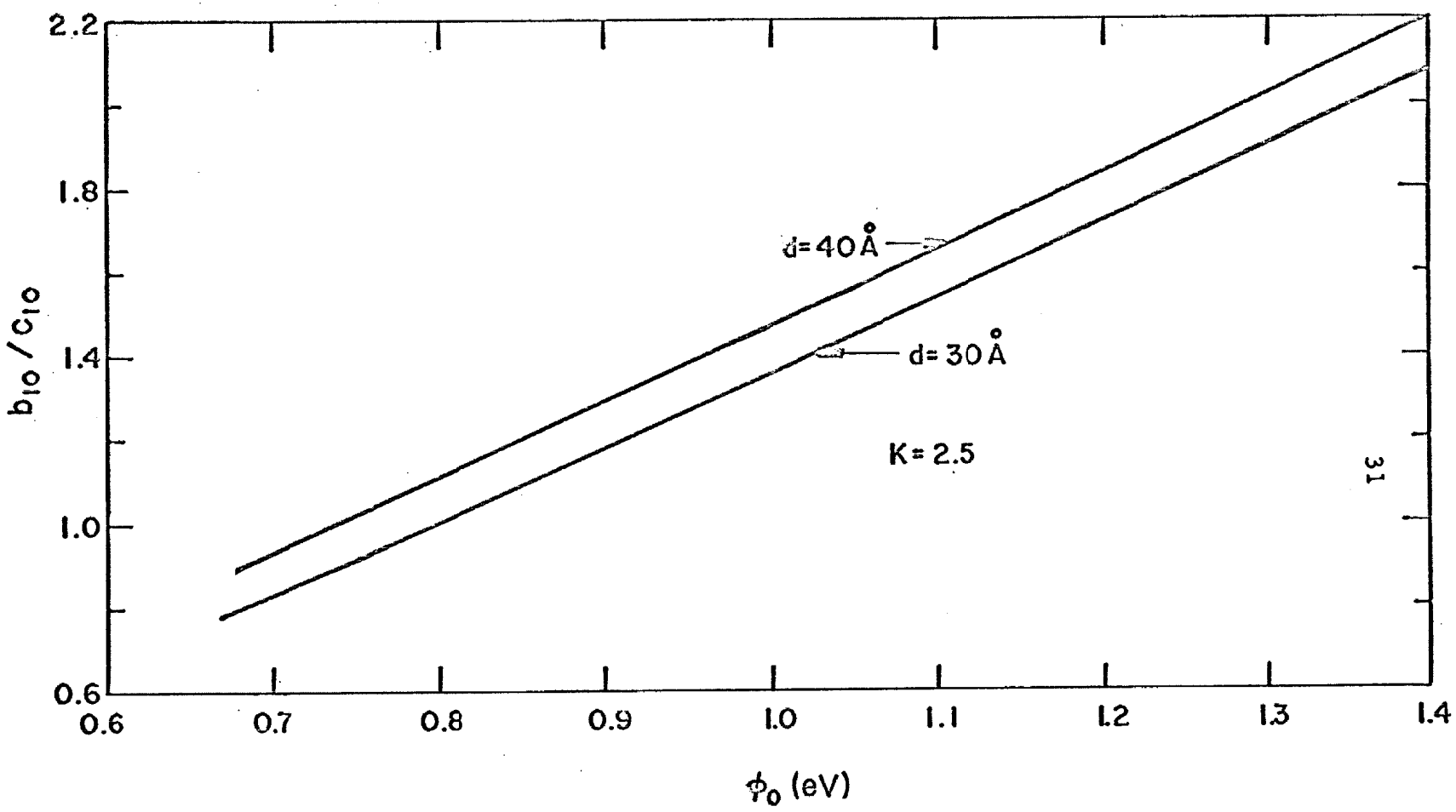

Fig. 5(e). Functional dependence of b_{10}/c_{10} on φ_0 as computed from equations 68 through 71.

clude only a qualitative derivation of its self energy as given by Fröhlich.[15]

The energy of an electric field in an isotropic dielectric medium of dielectric constant K is

$$W = \frac{1}{4\pi K} \int D^2 d\tau \tag{72}$$

in terms of the displacement D. Figure 6 shows the assumed potential for the electron. Outside a critical distance r_o the potential is essentially a classical Coulomb potential, but inside for simplicity it is taken as constant. From equation 72 the self energy of the electron is

$$W = \frac{e^2}{K r_o} \tag{73}$$

The static dielectric constant K_o is defined by

$$D = K_o \cdot E \tag{74}$$

where

$$D = E + 4\pi P \tag{75}$$

The total polarization field P can be split up into two components, the electronic polarization P_e and the ionic polarization P_I;

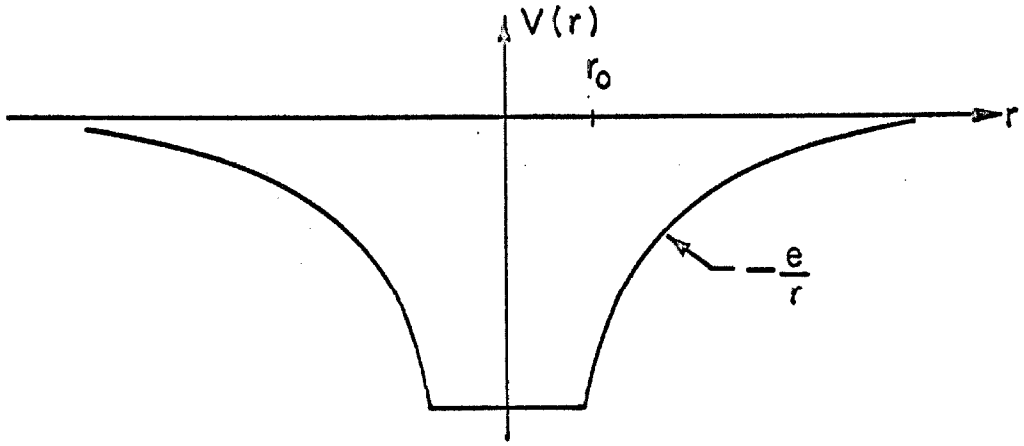

Fig. 6. Assumed potential energy diagram of an electron in an ionic insulator.

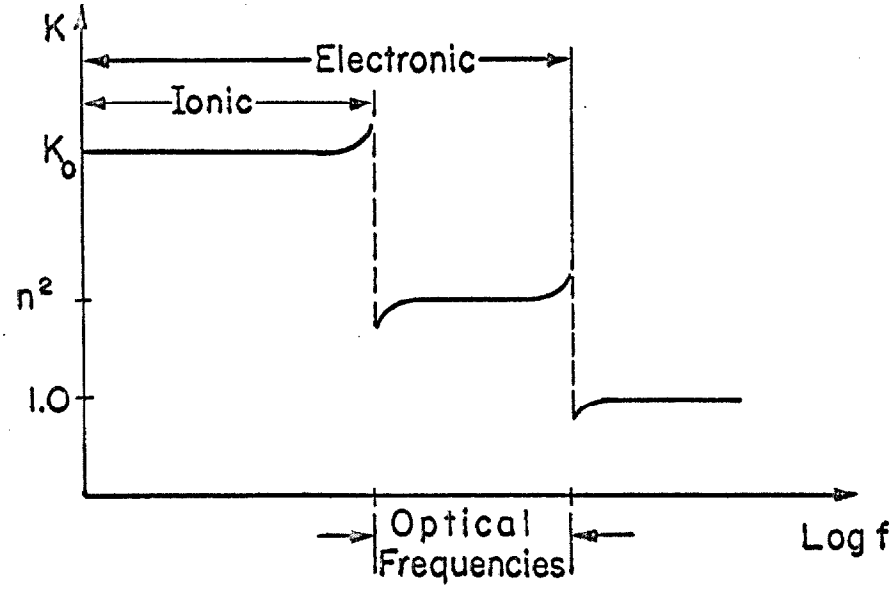

Fig. 7. Schematic diagram of the dielectric constant as a function of frequency. The value n is the optical index of refraction.

$$P = P_e + P_I \tag{76}$$

P_e and P_I correspond to optical and infrared resonances, respectively, as shown schematically in Fig. 7, where K is plotted as a function of frequency. If by some agency the electron was not interacting with the ions, the dielectric constant used in equation 73 would be n^2. Therefore the ionic contribution alone to the self energy is

$$\Delta W = -\left(\frac{1}{n^2} - \frac{1}{K_o}\right)\frac{e^2}{r_o} \tag{77}$$

The critical distance or polaron radius r_o is found by the uncertainty principle

$$r_o \approx \frac{2\pi\hbar}{mv} \tag{78}$$

or

$$\Delta W = -e^2\left(\frac{1}{n^2} - \frac{1}{K_o}\right)\frac{mv}{2\pi\hbar} \tag{79}$$

This implies that the potential lowering increases with the velocity of the electron. However, above a certain limiting velocity the ions will not be able to respond.

Spatially the ions that contribute the most to ΔW are the ones closest to the electron. An ion a distance r_o away witnesses an angular velocity due to the electrons motion of approximately v/r_o. This must be less than its highest ionic resonance or reststrahlen

frequency ω in order that these ions will be able to respond to the moving electron. Taking ω as the order of magnitude

$$v \approx r_o \omega \tag{80}$$

or from equation 78

$$v = \sqrt{\frac{2\pi\hbar\,\omega}{m}} \tag{81}$$

and

$$r_o = \sqrt{\frac{2\pi\hbar}{m\omega}} \tag{82}$$

Equation 79 becomes

$$\Delta W = -e^2\left(\frac{1}{n^2} - \frac{1}{K_o}\right)\sqrt{\frac{m\omega}{2\pi\hbar}} \tag{83}$$

Quantum mechanical field theory gives for ΔW[16]

$$\Delta W = -\left[\alpha + b\left(\frac{\alpha}{10}\right)^2 + \ldots\right]\hbar\omega \tag{84}$$

for

$$\alpha < 6$$

where

$$\alpha = e^2\left(\frac{1}{n^2} - \frac{1}{K_o}\right)\sqrt{\frac{m^*}{2\omega\hbar^3}} \tag{85}$$

$$= 3.69\left(\frac{1}{n^2} - \frac{1}{K_o}\right)\sqrt{\frac{m^*/m}{\hbar\omega}} \quad ; \hbar\omega \text{ in eV units}$$

α is a dimensionless coupling constant and b varies slightly with the method of computation but can be taken here as unity. The effective mass of the polaron is[16]

$$\frac{m_p^*}{m^*} = 1 + \frac{\alpha}{6} + 0\left(\frac{\alpha}{10}\right)^2 \qquad (85.a)$$

In light of the above, the conduction band in an ionic crystal will be considered the band in which an electron can exist in a highly excited state or is traveling at a sufficient velocity so as to produce no localized distortion of the crystal, consistent with non-polar crystal theory. For sufficiently slow electrons, allowed states exist below the band, or in other terms, the polaron conduction band is displaced downward by an amount $|\Delta W|$ from the electron conduction band.

A second deviation from non-polar crystals can be seen in the energy level diagram of NaCl shown in Fig. 8.[17] The energy levels are best described in terms of the individual ions with the splitting into bands as a perturbation. That is, when requiring the periodic Bloch wave functions

$$x(\vec{r}) = \pi(\vec{r}) \exp i\vec{k} \cdot \vec{r} \qquad (86)$$

to be solutions, $\pi(\vec{r})$ is the dominant factor and $\exp i\vec{k} \cdot \vec{r}$ is a perturbation. This leads to narrow allowed bands and high effective masses.[18] If this were the case for the conduction band under

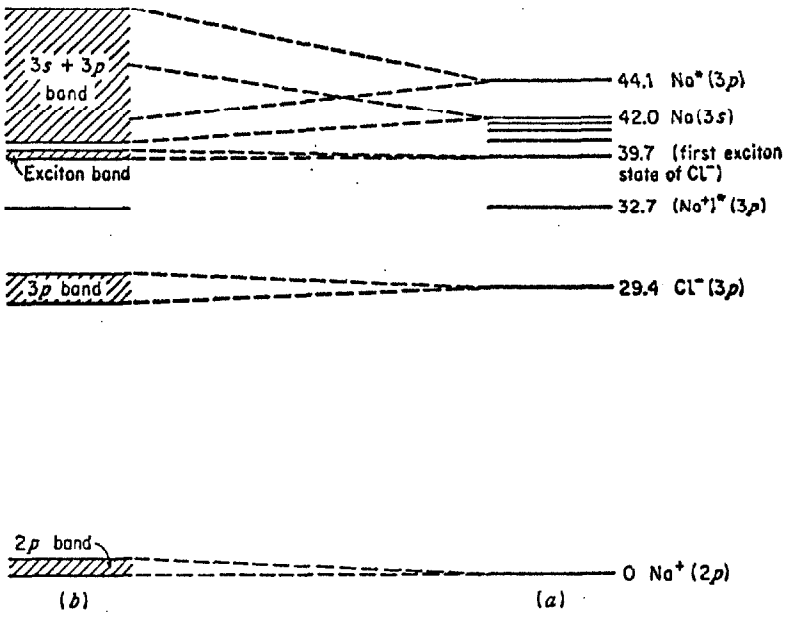

Fig. 8(a). Discrete energy levels of the NaCl crystal. (b). Typical broadening into energy bands when the interactions between the ions are taken into account. The ordinate is in units of electron volts. The abscissa represents the distance between the ions, with (b) occurring at the equilibrium separation r_o (after Sachs[17]).

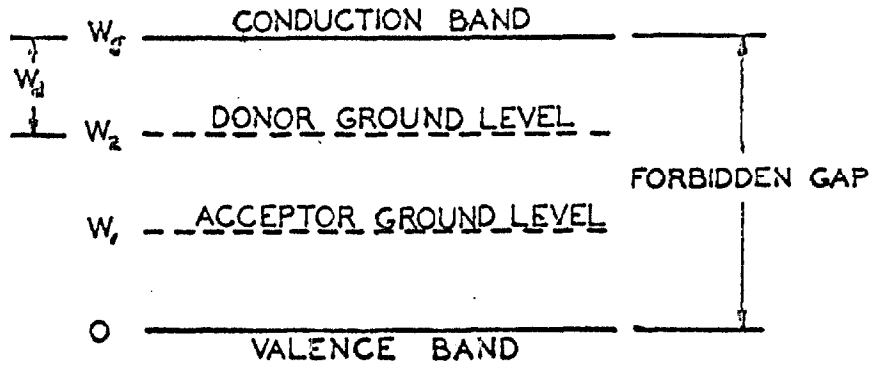

Fig. 9. Energy level diagram of trapping states in the forbidden gap.

study, the WKB plane-wave approach used in the analysis of metal-insulator injection would be in serious error and metal-to-metal tunneling in some doubt, in particular when computing the imaginary momentum (equation 6) the energies might be referenced to some other level rather than the bottom of the insulator conduction band.

1.4 Frenkel Effect

Frenkel[7] has proposed a conduction mechanism in which free electrons are created by thermal ionization of deep traps in high electric fields. This mechanism could be called a Schottky bulk mechanism because it is very similar to the reduction of the work function at a metal surface by the image force. Here, however, the electron is escaping from a localized atom, and the positively charged ion left behind is immobile. This gives rise to a thermal activation energy lowering of

$$\Delta\varphi_o = 2\left(\frac{e^3F}{K}\right)^{1/2} \qquad \text{Frenkel} \qquad (87)$$

Whereas in the first section of this chapter, it was shown the lowering at an electrode is

$$\Delta\varphi_o = \left(\frac{e^3F}{K}\right)^{1/2} \qquad \text{Schottky} \qquad (88)$$

Assuming one knows K, these competing mechanisms would be

experimentally discernible if the location of the Fermi level with respect to the trapping level or levels were known. This problem is discussed by Kittel[19] in the following manner.

Figure 9 shows the energy level diagram where zero energy is now taken at the top of the valence band. Let N_d and N_a be the concentrations of the donor and acceptor atoms, respectively, and the superscript "o" designate the unionized, + or - the ionized donors and acceptors; i.e.,

$$N_d = N_d^{o} + N_d^{+} \tag{89}$$

$$N_a = N_a^{o} + N_a^{-} \tag{90}$$

then

$$N_d^{o} = \frac{N_d}{1 + \exp(W_2 - W_F)/kT} \tag{91}$$

$$N_a^{o} = \frac{N_a}{1 + \exp -(W_1 - W_F)/kT} \tag{92}$$

and

$$N_d^{+} = N_d - N_d^{o} = \frac{N_d}{1 + \exp -(W_2 - W_F)/kT} \tag{93}$$

$$N_a^{-} = N_a - N_a^{o} = \frac{N_a}{1 + \exp (W_1 - W_F)/kT} \tag{94}$$

Charge neutrality requires

$$p + N_d^+ = n + N_a^- \tag{95}$$

where p and n are the hole and electron concentrations in the valence and conduction band respectively. Considering the holes and electrons in their respective bands behaving as if they were free,

$$p = n_+^o \exp -W_F/kT \tag{96}$$

$$n = n_-^o \exp (W_F - W_g)\, kT \tag{97}$$

where

$$n_+^o = 2(2\pi m_h kT/h^2)^{3/2} \tag{98}$$

$$n_-^o = 2(2\pi m_e kT/h^2)^{3/2} \tag{99}$$

are the effective density of states in the valence and conduction band. At room temperature and for $m_h = m_e$ = mass of a free electron, $n_+^o = n_-^o = 2.5 \times 10^{19}$ cm^{-3}. Equations 93 through 99 determine the Fermi energy level W_F.

Assuming for the moment there are no acceptors present, $N_a = 0$. Furthermore for

$$\exp (W_F - W_g)/kT> > \exp -W_F/kT \tag{100}$$

that is, for W_F above $W_g/2$, $n > > p$ by equations 67 and 68. Under these assumptions equations 93, 95 and 97 combine to

$$\frac{N_d}{1 + \exp -(W_2 - W_F)/kT} = n_-^o \exp (W_F - W_g)/kT \tag{101}$$

from which W_F is found by rewriting as

$$\exp W_F/kT = \frac{[\,1 + 4(N_d/n_-^o)\exp (W_g - W_2)/kT]^{1/2} - 1}{2\exp(-W_2/kT)} \tag{102}$$

W_F may be found in two limits. If

$$4\left(\frac{N_d}{n_-^o}\right) \exp \left(\frac{W_g - W_2}{kT}\right) << 1 \tag{103}$$

then

$$W_F \approx W_g + kT \ln \frac{N_d}{n_-^o} \tag{104}$$

which means from equation 97 that

$$n \approx N_d \tag{105}$$

or that the number of conduction electrons is equal to the number of donors. This is normally the case for semiconductors at room temperature. The second limit

$$4\left(\frac{N_d}{n_-^o}\right) \exp (W_g - W_2)/kT >> 1 \qquad (106)$$

corresponds to an insulator with a large number of deep traps. That is,

$$W_d = W_g - W_2 \qquad (107)$$

is the donor ionization or activation energy and is large with respect to kT. Now

$$W_F \approx \frac{W_g + W_2}{2} + \frac{kT}{2} \ln \frac{N_d}{n_-^o} \qquad (108)$$

and

$$n = (n_-^o N_d)^{1/2} \exp -W_d/2kT \qquad (109)$$

This is the result given by most authors, see for instance Spenke.[20] Kittel feels that it is an artificial one because of the assumption that the number of acceptor atoms can be neglected when talking about so few conduction electrons. These acceptors are filled up from the donor atoms and move the Fermi level down to W_2 whereby

$$n \propto \exp -W_d/kT \qquad (110)$$

The result is that there are two possibilities for the Frenkel effect; one

$$\sigma = \sigma_o \exp\left[\left(\frac{e^3 F}{K}\right)^{1/2}/kT\right] \qquad (111)$$

where there are only donor levels and these are essentially full;

and the other,

$$\sigma = \sigma_o \exp\left[2 \left(\frac{e^3 F}{K} \right)^{1/2} / kT\right] \qquad (112)$$

where there are acceptors present also.

CHAPTER II

EXPERIMENTAL RESULTS

The diodes were constructed by first depositing aluminum on a sheet of mica that has been cleaved in the vacuum just prior to the evaporation. After removal from the vacuum system, copper leads were soldered to the aluminum surface and a glass block bonded to the surface as a backing for support. The sample was then returned to the vacuum system and the mica stripped off the glass block leaving behind a thin film of mica on the aluminum. Gold dots were then immediately deposited on this freshly cleaved mica surface. This procedure resulted in an Al-mica-Au sandwich in which both mica interfaces were produced at cleavage planes never exposed to the atmosphere. Because the thickness of the mica was not the same over the entire sample but uniform only over relatively small and irregular patches, small dots of the order of 10^{-4} cm^2 in area were chosen so that several diodes of the same thickness were available. This made it possible not only to have many diodes of the same thickness to work with in case one was destroyed, but it also insured that some part of a dot was not straddling a step in the mica; that is, no volt-ampere data was taken unless a diode was completely surrounded by diodes of the same volt-ampere characteristics. Electrical contact was made mechanically to the dots by means of a fine gold

wire. The thickness of the mica was computed from the diode's capacitance, as measured on a bridge, and from the area of the dot, measured either directly by means of a probe attached to a micromanipulator or from photographs taken through a microscope. The volt-ampere data was taken at dc for temperatures between 77 and 373°K and for thicknesses from 30 to 11,600Å.

The photoelectric response was measured using larger areas of thin gold through which chopped monochromatic light of known intensity was beamed. The resultant current was then synchronously detected with the diode under bias.

The dependence of the current on voltage and temperature can be classified by the thickness of the mica films. The 30 and 40Å volt-ampere curves showed tunneling current with the voltage dependence of equation 61, $j = G(T)[V + (c_{10}^2/24 - b_{12})V^3]$, and the weak temperature dependence to be expected of this mechanism. However, for thicknesses of 50Å and greater at room temperature the current was proportional to $\exp\beta\sqrt{F}$ and strongly temperature dependent as in Schottky emission. Only at lower temperatures did the current become temperature independent.

2.1 Metal-to-Metal Tunneling, Very Thin Films

It will now be shown that the current as a function of voltage and temperature for the 30 and 40Å films can be fitted quite closely to equations 61 and 62 for voltages less than φ_o, in which case

electrons tunnel from near the Fermi level of one metal directly to unoccupied states just above the Fermi level of the second metal. Figure 10 shows the volt-ampere characteristic at room temperature for a 40Å green muscovite sample. Since the diode has so little asymmetry, one can attempt to analyze this data in terms of the symmetrical diode equations derived in Chapter I. The data of Fig. 10 show a linear characteristic at low voltages or a "tunneling resistance" R = V/I of $2.31 \times 10^8 \Omega$. With this value, Fig. 12 is constructed for the aluminum-positive data by subtracting out the ohmic dependence. As shown, (I-V/R) has a cubic dependence on voltage over a wide range, departing only at larger values as higher powers of V become important. The cubic dependence yields

$$\frac{1}{24} c_{10}^{\,2} - b_{12} = 21.1$$

from equation 61. From considerations of the temperature data discussed later it will be shown b_{12} is negligible in comparison to $c_{10}^{\,2}/24$, and thus

$$c_{10} = 22.5$$

Using equations 59 and 62,

$$b_{10} = 31.1$$

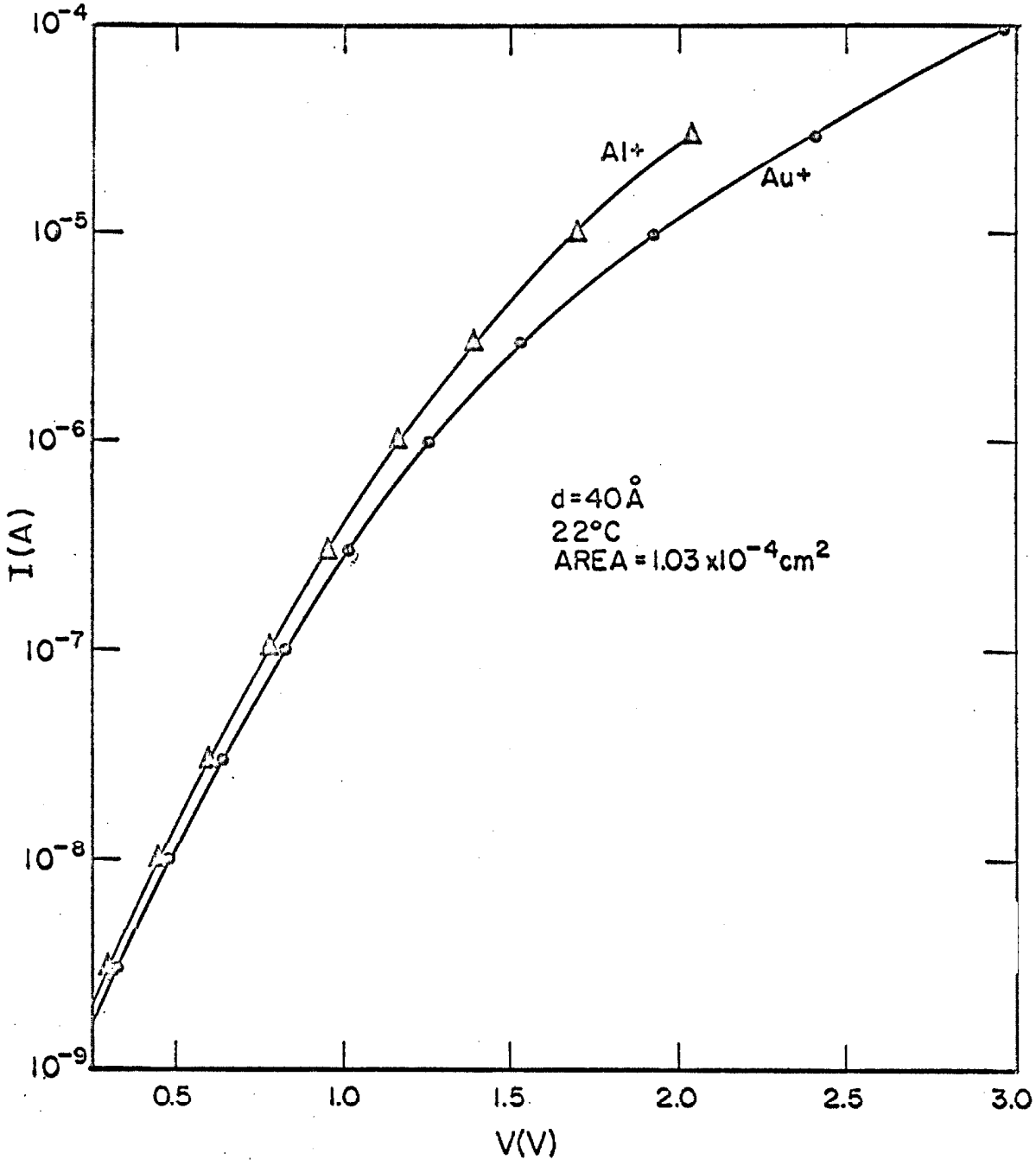

Fig. 10. Volt-ampere characteristic of a 40Å green muscovite film. The tunneling resistance is 2.31 x 10^8 Ω.

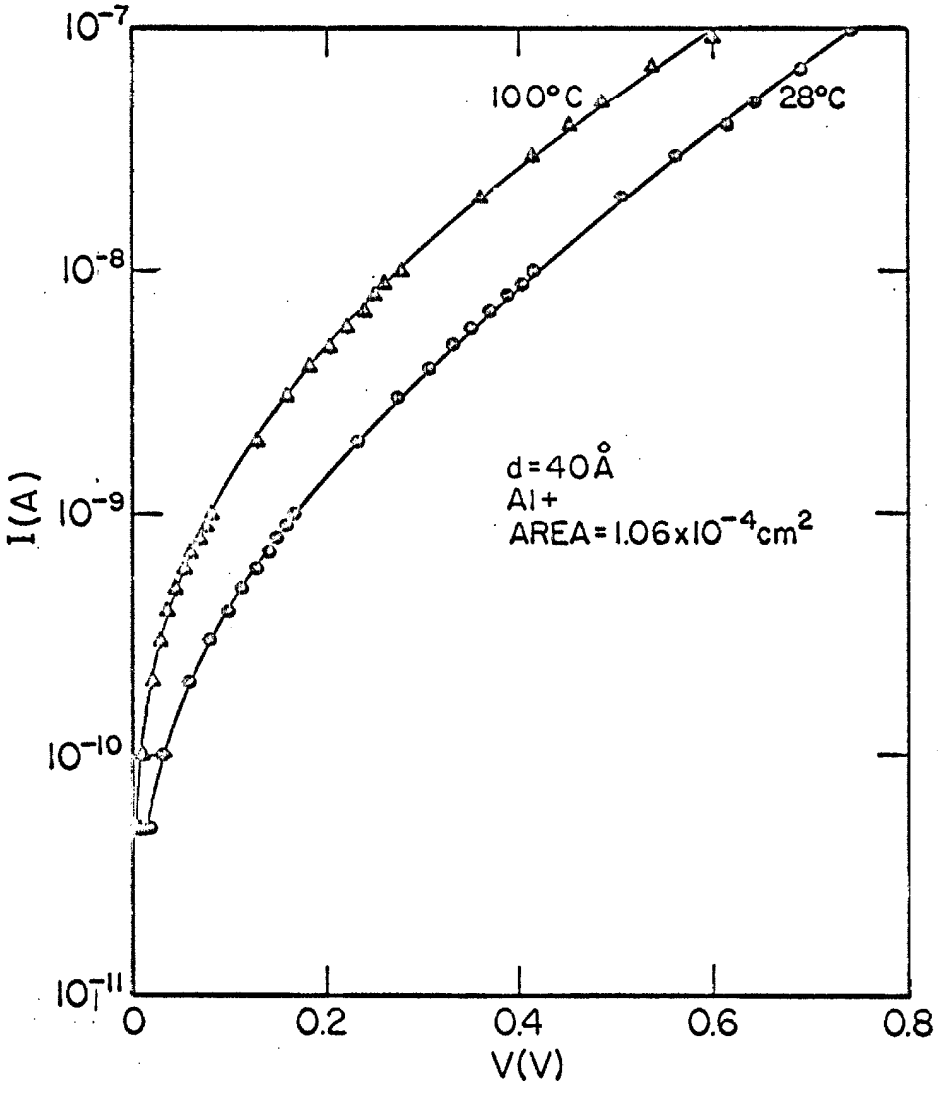

Fig. 11. Volt-ampere characteristic of a 40Å green muscovite film.

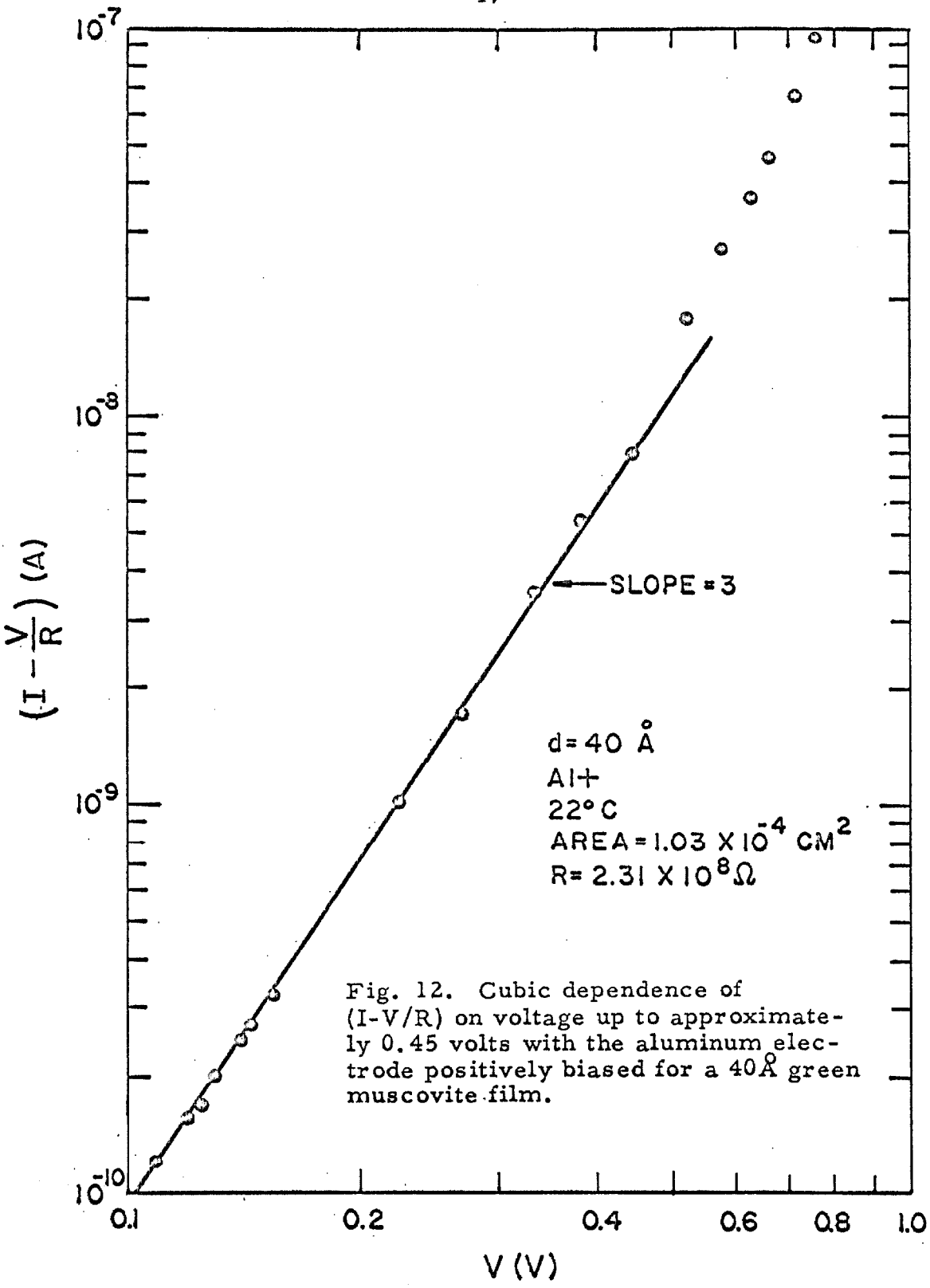

Fig. 12. Cubic dependence of (I-V/R) on voltage up to approximately 0.45 volts with the aluminum electrode positively biased for a 40Å green muscovite film.

and hence from Fig. 5e the barrier height is

$$\omega_o = 0.95eV$$

which yields

$$\frac{m^*}{m} = 0.92$$

from Figs. 5a or 5b. The forward and reverse characteristics of a diode having two different metal-insulator barrier heights would have a V^2 term in equation 61.[9] Instead of this appearing in the volt-ampere data for both biases, an anomalous $V^{3.49}$ term replaces the expected cubic power in V for the gold side positively biased as shown in Fig. 13. The reasons for this behavior are not understood, but it would appear that the asymmetry of the data does not arise from any significant difference in barrier heights at the two interfaces. However, forcing a slope of three in Fig. 13 results in $c_{10} = 19.1 \pm 3.2$ versus the 22.5 obtained from the aluminum-positive data.

The temperature variation as expressed in the coefficient $(\pi c_{10} kT)/\sin(\pi c_{10} kT)$ of equation 62 allows one to calculate an independent value of c_{10}. Experimentally the value of R at 77.4°K is larger than the room temperature (295°K) value by a factor of 1.77. This factor yields the same value of $c_{10} = 22.5$, confirming that b_{12} is negligible. On the other hand the current at 373°K is a factor of 1.98 too large so that one might conclude that the condition of

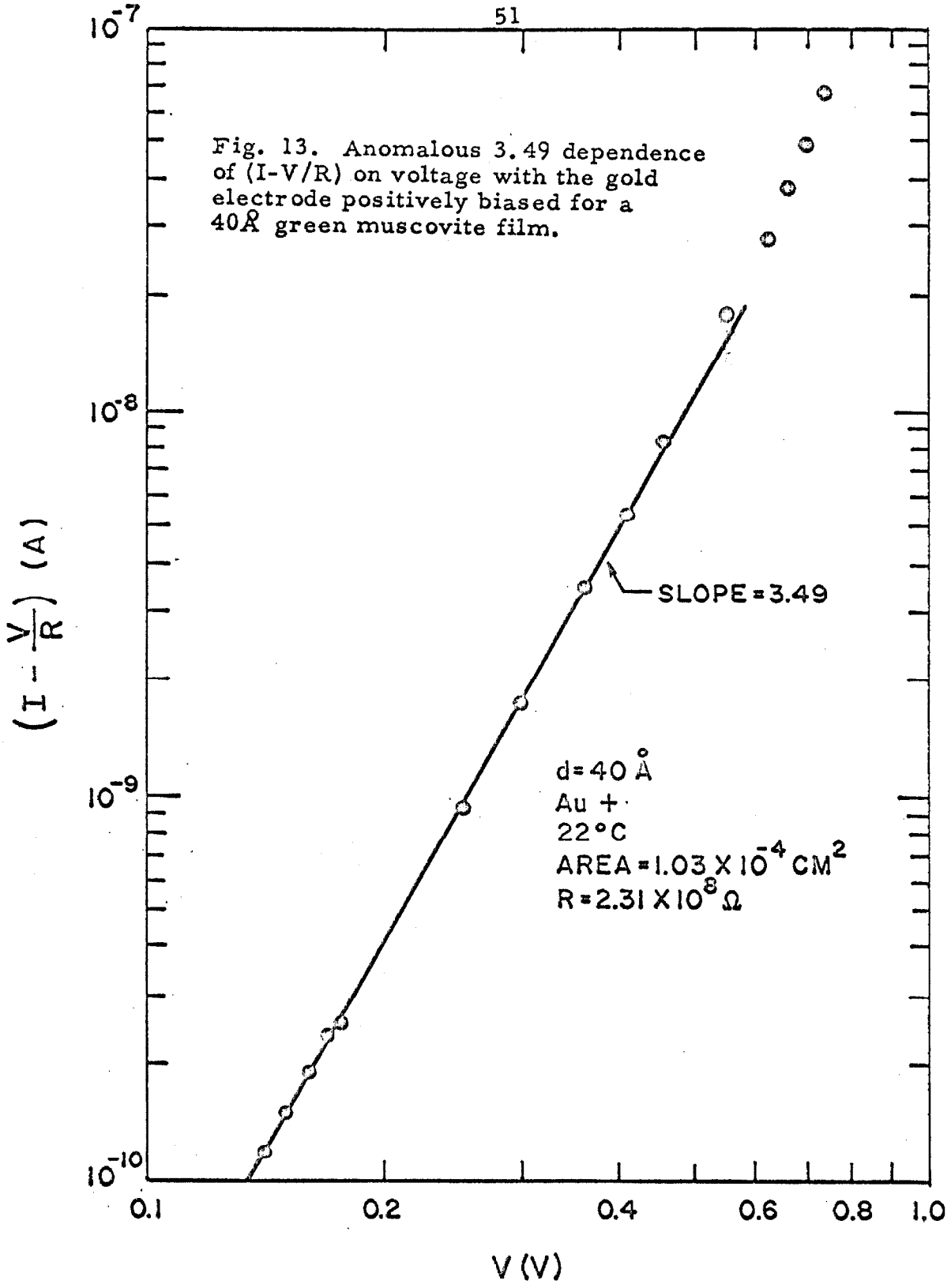

Fig. 13. Anomalous 3.49 dependence of (I-V/R) on voltage with the gold electrode positively biased for a 40Å green muscovite film.

equation 54 is not being satisfied at this higher temperature. This corresponds to a value of f_1 greater than 37.5, a value unobtainable from equation 51 for a pure image-force barrier shape. Hartman has observed data on Al-Al_2O_3-Al structures which suggest that the classical turning points x_1 and x_2 are anomalously closer to the metallic faces and the image force weaker, such that both f_1 and b_{12} are larger than anticipated.[21] This situation may also be the case here.

Similar curves for 30Å green muscovite are shown in Figs. 14 and 15. Temperature data yield 12.6 for c_{10}. However from Fig. 15

$$\frac{1}{24} c_{10}^2 - b_{12} = 0.76$$

which means b_{12} is not negligible here, whereas it was for the 40Å film. A departure from the true image-force barrier shape near the electrodes would be more important for a thinner film and may explain this difference. On the other hand substituting the experimental tunneling conductance $G(295^{\circ}K) = 0.549 \Omega cm^{-2}$ and $c_{10} = 12.6$ into equation 59 and 62, one obtains $b_{10} = 21.7$. This would imply $\varphi_o = 1.2eV$ and $m^*/m = 0.65$, which is unreasonable. However, taking $m^*/m = 0.92$ as in the 40Å film and $b_{10} = 21.7$,

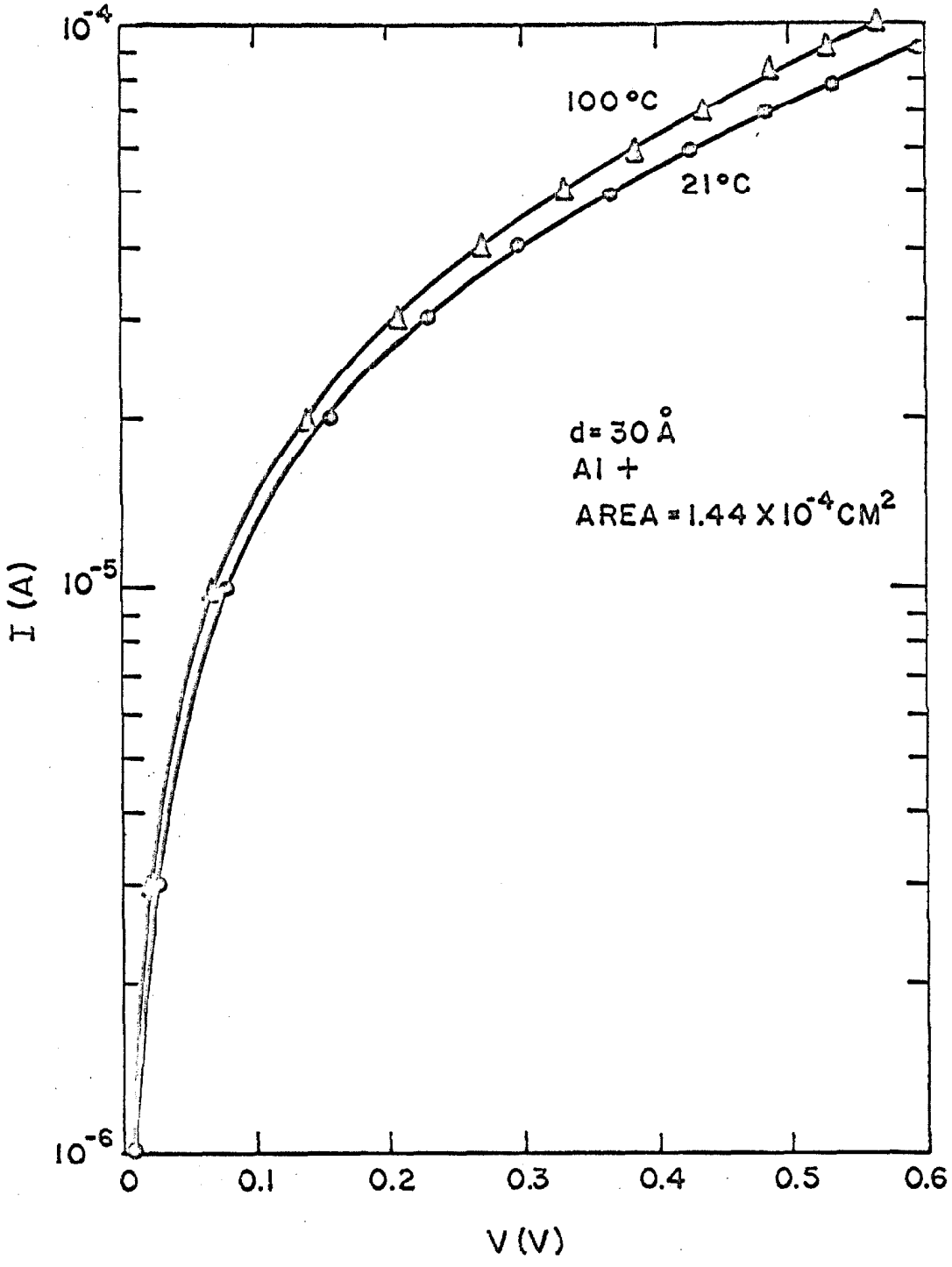

Fig. 14. Volt-ampere characteristic of a 30Å green muscovite film.

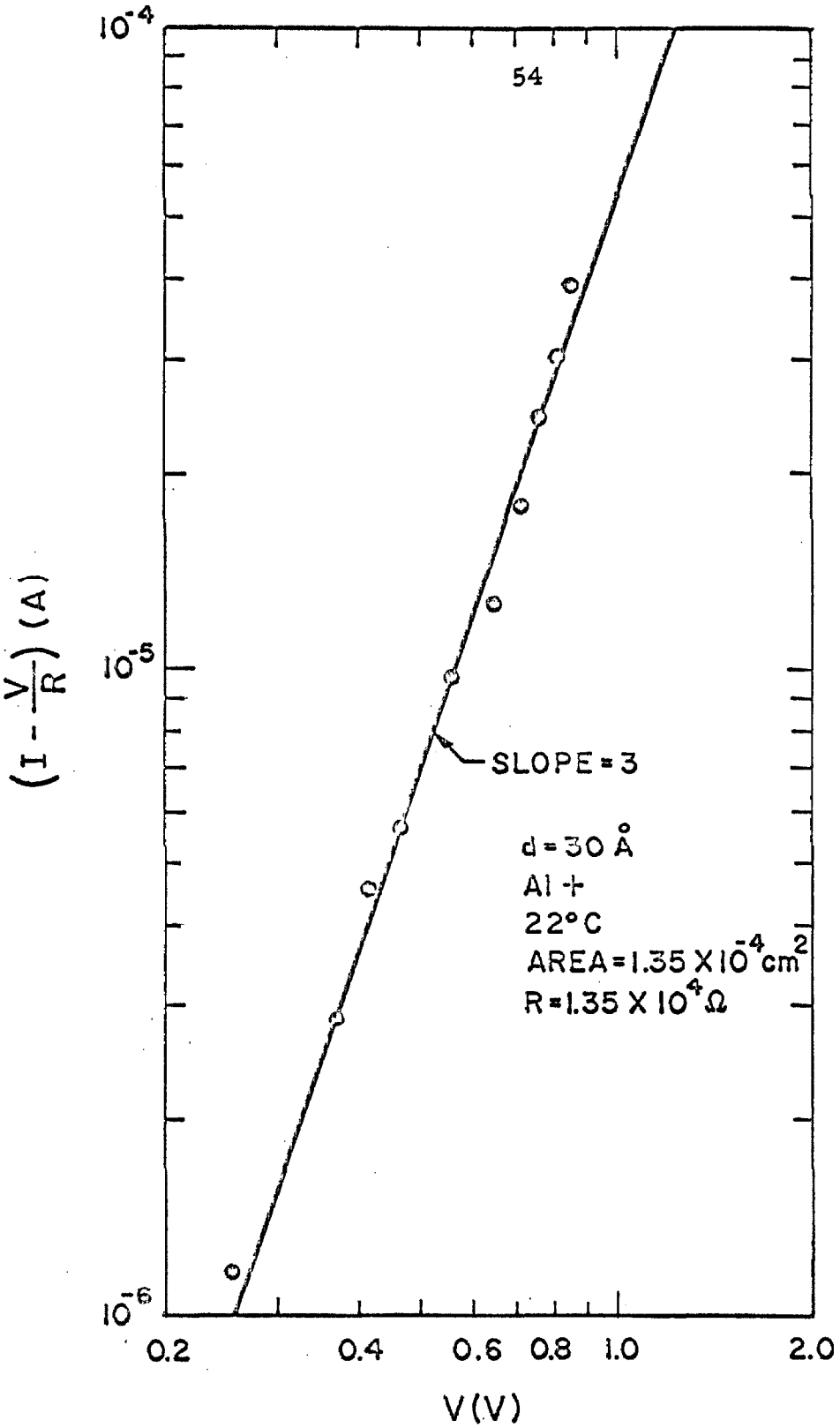

Fig. 15. Cubic dependence of (I-V/R) on voltage for a 30Å green muscovite film. Volt-ampere data was symmetrical with respect to bias.

$$\varphi_o = 0.93\text{eV}$$

in good agreement with 0.95eV found for the 40Å film. On the other hand these values mean that c_{10} should be 17.5, which is in considerable disagreement with 12.6. Because, however, the V-I curves of the 30Å films had a more rapid drift rate than the 40Å data (noticeable in hours rather than months, respectively), particularly in the non-ohmic region, they can only be considered an approximate check on the 40Å results.

Thicknesses of 10 and 20Å presumably were encountered but appeared as dead shorts on the capacitance bridge because of their very low impedance. Also several samples of thin ruby muscovite were tested and, although no analysis of the above type was attempted, their lower tunneling resistance would indicate they had a slightly lower barrier height than the green muscovite.

The above effective mass ratio being close to unity is to be expected in a large forbidden gap,[22] such as the 4eV gap found in muscovite.[23] The argument is briefly that the form of the wave vector near the center of a wide conduction band[24] is similar to that of its imaginary counterpart in a wide forbidden gap. Table III compares the values of φ_o and m^*/m calculated from b_{10}=31.1 and b_{11} = 11.26 using the barrier shapes suggested by Stratton to those using the actual image-force potential. Of the three approximations, the rectangular barrier appears to fit the actual image-force

barrier shape the best.

Table III

$d = 40\text{Å}$ $K = 2.5$ $b_{10} = 31.1$ $b_{11} = 11.26$

Shape	φ_o(eV)	m^*/m
image-force	0.95	0.92
parabolic	1.48	0.746
triangular	2.17	0.668
rectangular	0.79	1.025

In Table IV, φ_o is calculated for $d = 30\text{Å}$ and $b_{10} = 21.7$ using the effective mass ratio arrived at in Table III for its respective barrier shape.

Table IV

$d = 30\text{Å}$ $K = 2.5$ $b_{10} = 21.7$

Shape	φ_o(eV) using	m^*/m
image-force	0.93	0.92
parabolic	1.39	0.746
triangular	2.00	0.668
rectangular	0.77	1.025

It can be seen by comparing Table IV with Table III, that this procedure is not a sensitive method for the determination of the barrier shape. With mica there is no reason to suspect that the

true image-force barrier shape is not the correct one.

2.2 Metal-to-Insulator Injection for Thick Films; Temperature Dependent Current

Thicker films of green muscovite at room temperature have linear ln I versus $\sqrt{V}$ curves highly suggestive of Schottky emission as shown in Figs. 16 and 17. From the slopes of Fig. 17 (drawn with the aid of the thicknesses d_c computed from capacitance measurements) the dielectric constant K can be calculated using equation 22. However, when this is attempted K turns out to be a function of thickness indicating that d_s, the thickness computed for a constant K from the Schottky slopes by means of equation 22, is not equal to d_c. Rather than using this approach to the problem, Fig. 18 was constructed wherein d_s has been set equal to ad_c+b, which is the simplest functional relationship that one could attempt to satisfy the experimental measurements, and K determined from the condition that $a = 1$. This procedure results in K being a constant equal to 3.28. Furthermore, the current density at a given temperature is essentially a function only of the field V/d as shown in Fig. 19 and 20, and expressed in equation 22. However, the reasons for the failure of the straight lines of Figs. 18, 19, and 20 to pass through the origin are not known at the present time.* Finally, the barrier height computed from room temperature and

---

* Figs. 18, 19 and 20 have been constructed from gold-positive data. Aluminum-positive data are very similar and offer nothing new.

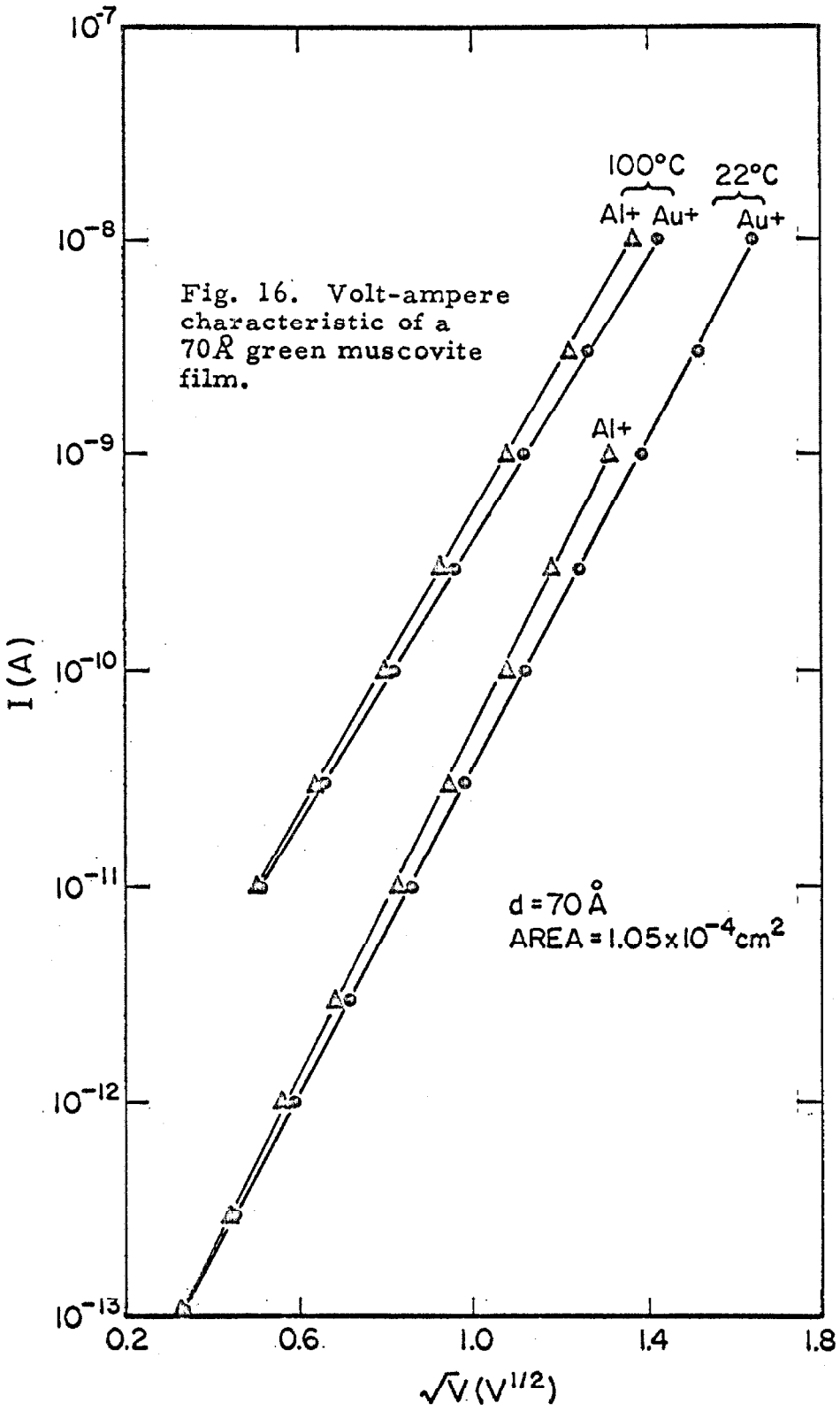

Fig. 16. Volt-ampere characteristic of a 70Å green muscovite film.

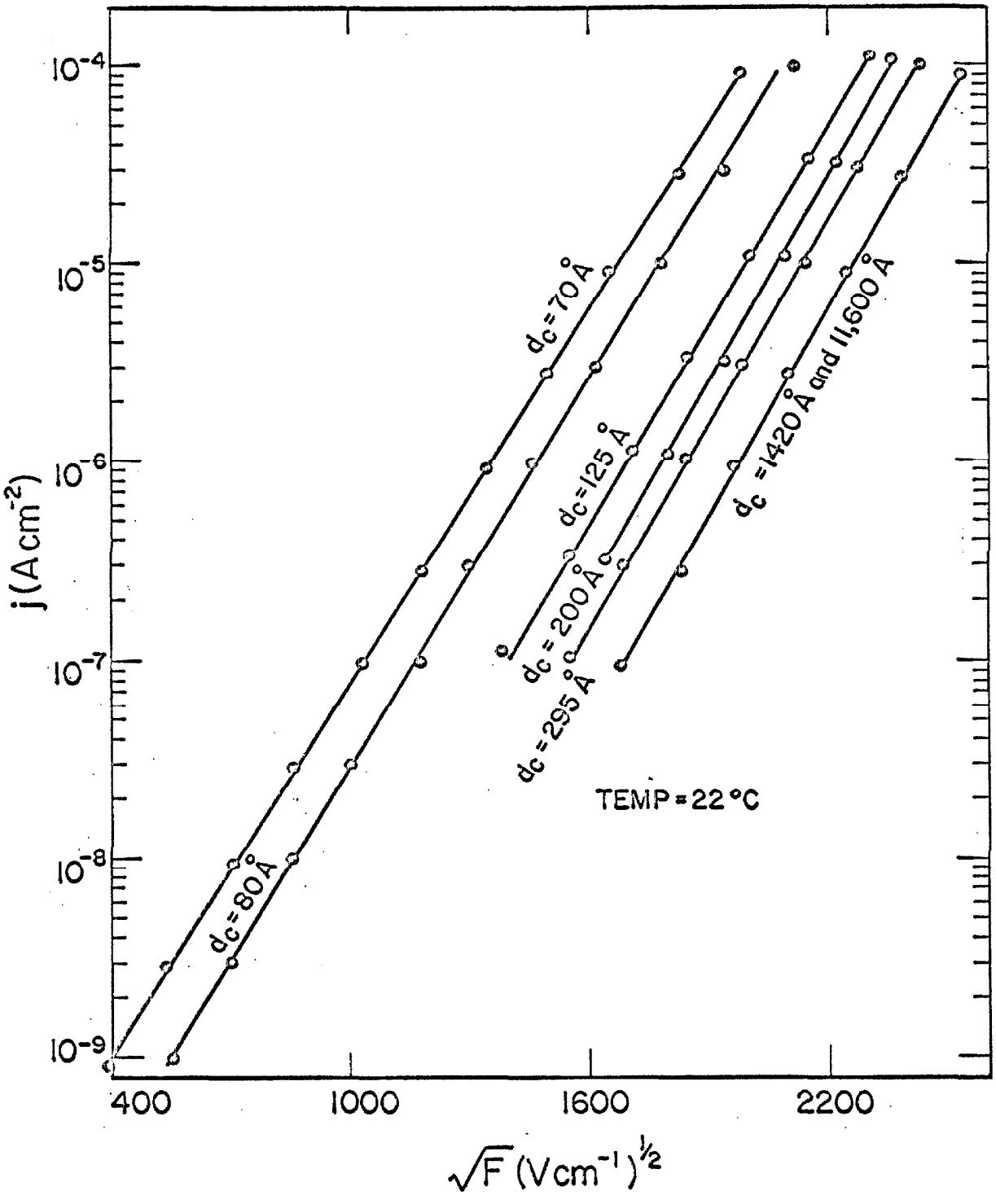

Fig. 17. Current density versus the square root of the applied field for green muscovite.

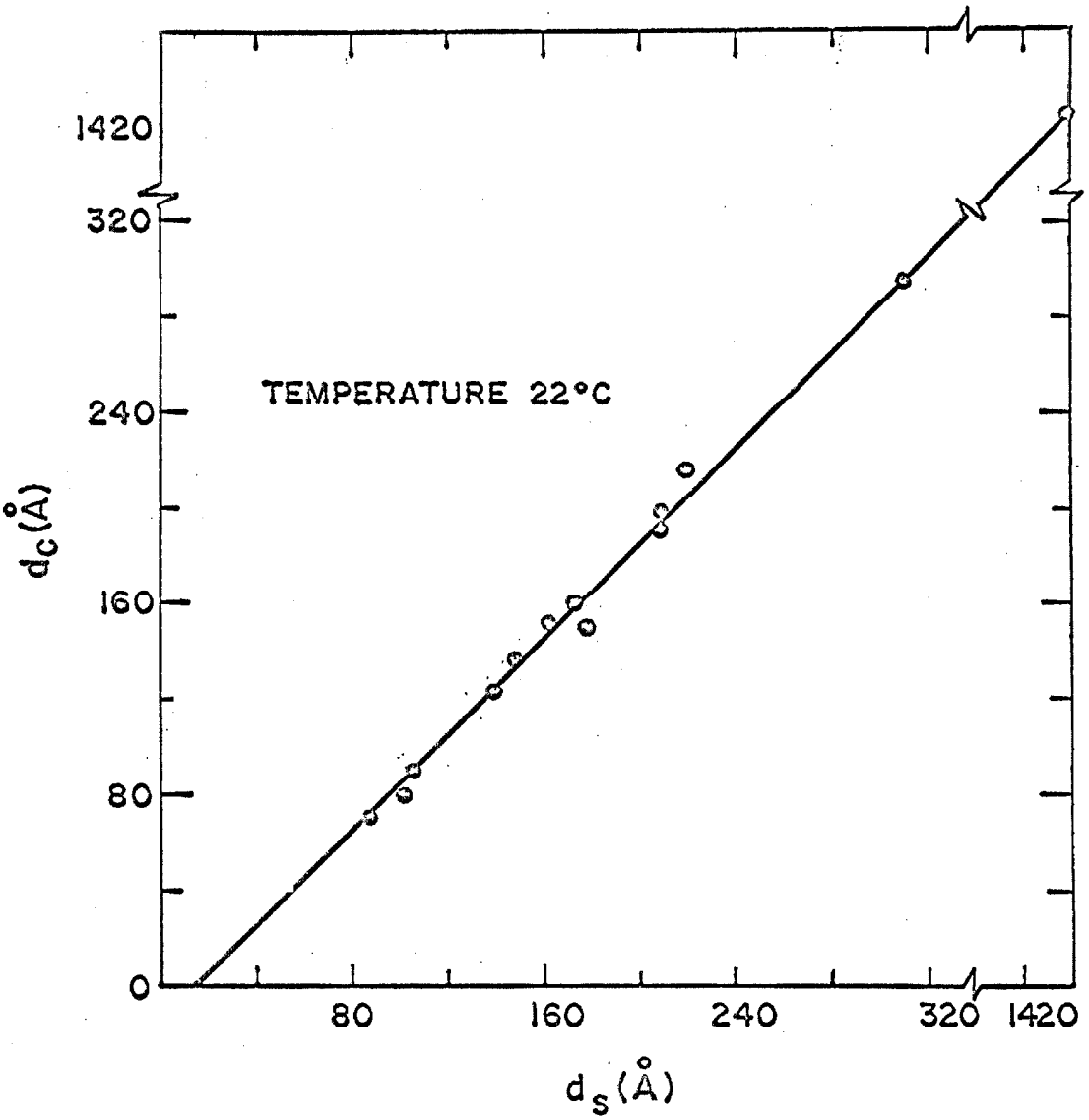

Fig. 18. Thickness d_c, calculated from capacitance, versus d_s, calculated from Schottky slopes for K = 3.28, as explained in the text. Material is green muscovite.

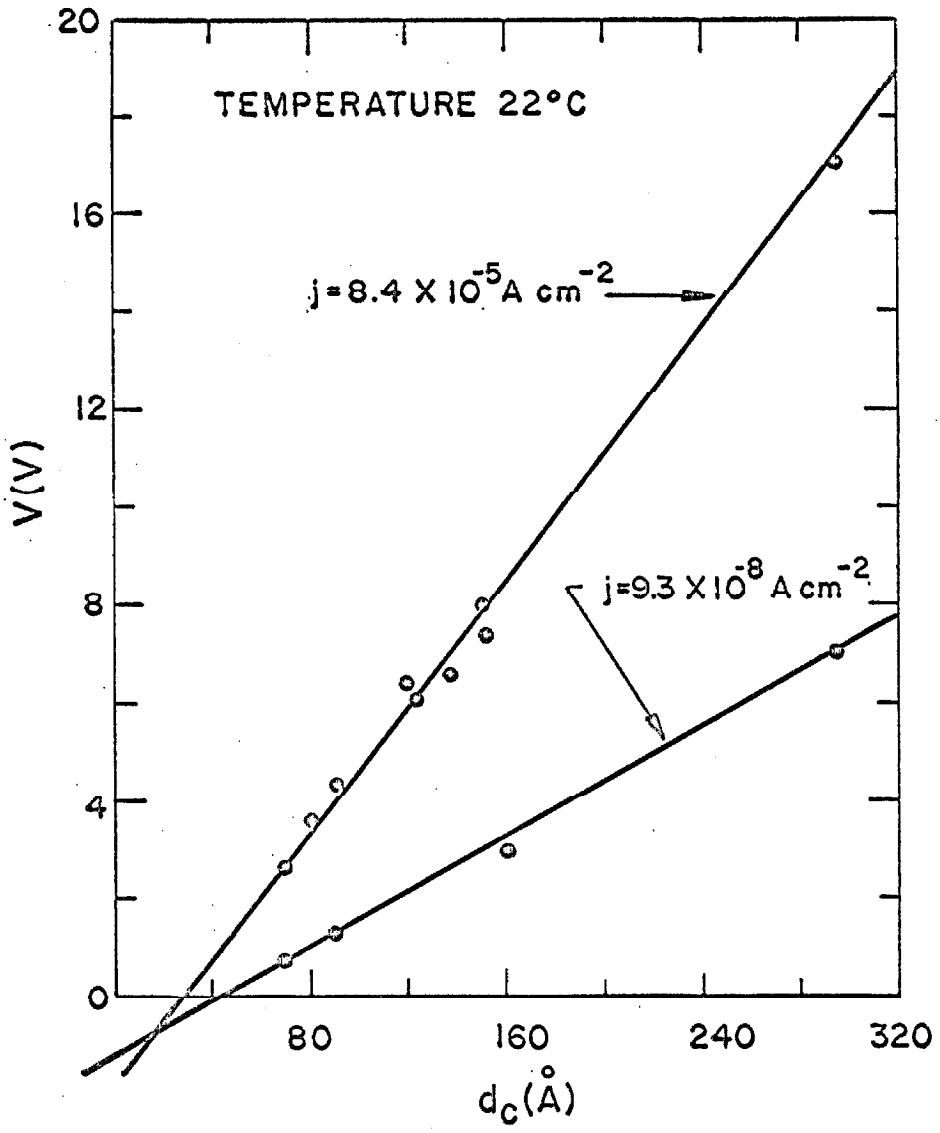

Fig. 19. Voltage for a constant current density versus thickness computed from capacitance. Material is green muscovite.

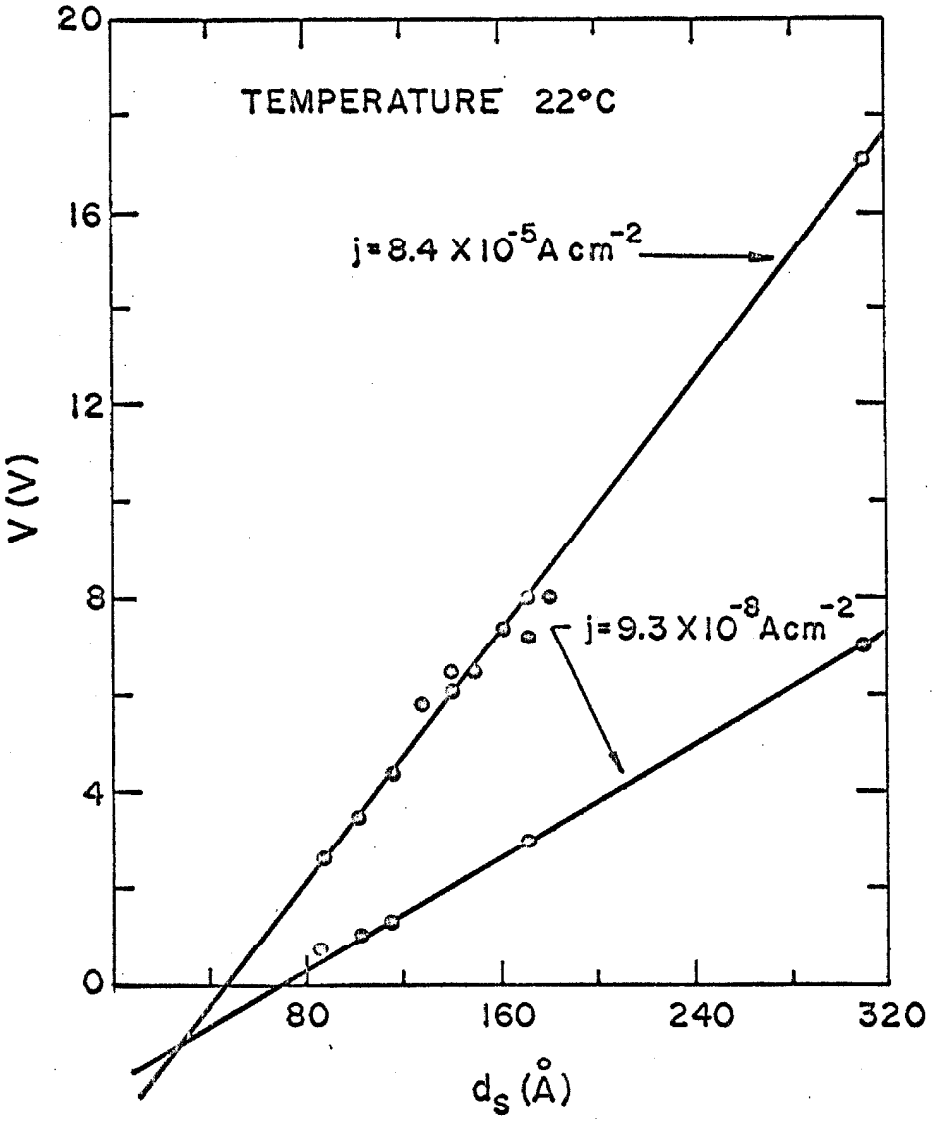

Fig. 20. Voltage for a constant current density versus thickness calculated from Schottky slopes for K = 3.28. Material is green muscovite.

100°C data using equation 22 approaches 0.55eV as shown in Fig. 21. The fact that it is not a constant may possibly be associated with the non-zero intercept problem.

With the exception of these discrepancies, the picture is consistent with Schottky emission into a polaron conduction band since the dielectric constant K is above its optical value of $n^2 = 2.5$, and the energy of the injected electron is apparently 0.4eV below the bottom of the electron conduction band found from the quick transition process of metal-to-metal tunneling.[25] In equations 84 and 85 with $|\Delta W| = 0.4$eV, $K_o = 3.28$, $n^2 = 2.5$, and $\hbar\omega = 0.10$eV (the reststrahlen vibration energy of the SiO_4 group[26]), the effective mass ratio in the polaron conduction band would be 13. However, further analysis of the data taken at 100°C sheds more light on this process and shows that this calculation must be somewhat refined.

The only essential difference in the data taken at 100°C is the polaron dielectric constant decreased to 2.83 from 3.28 due to the higher average velocity of the electrons. This is a large enough change to have an important effect in the lowering of the polaron conduction band and more detailed temperature measurements should be taken. However, if the polaron model is correct, the situation is as shown in Fig. 22. Here

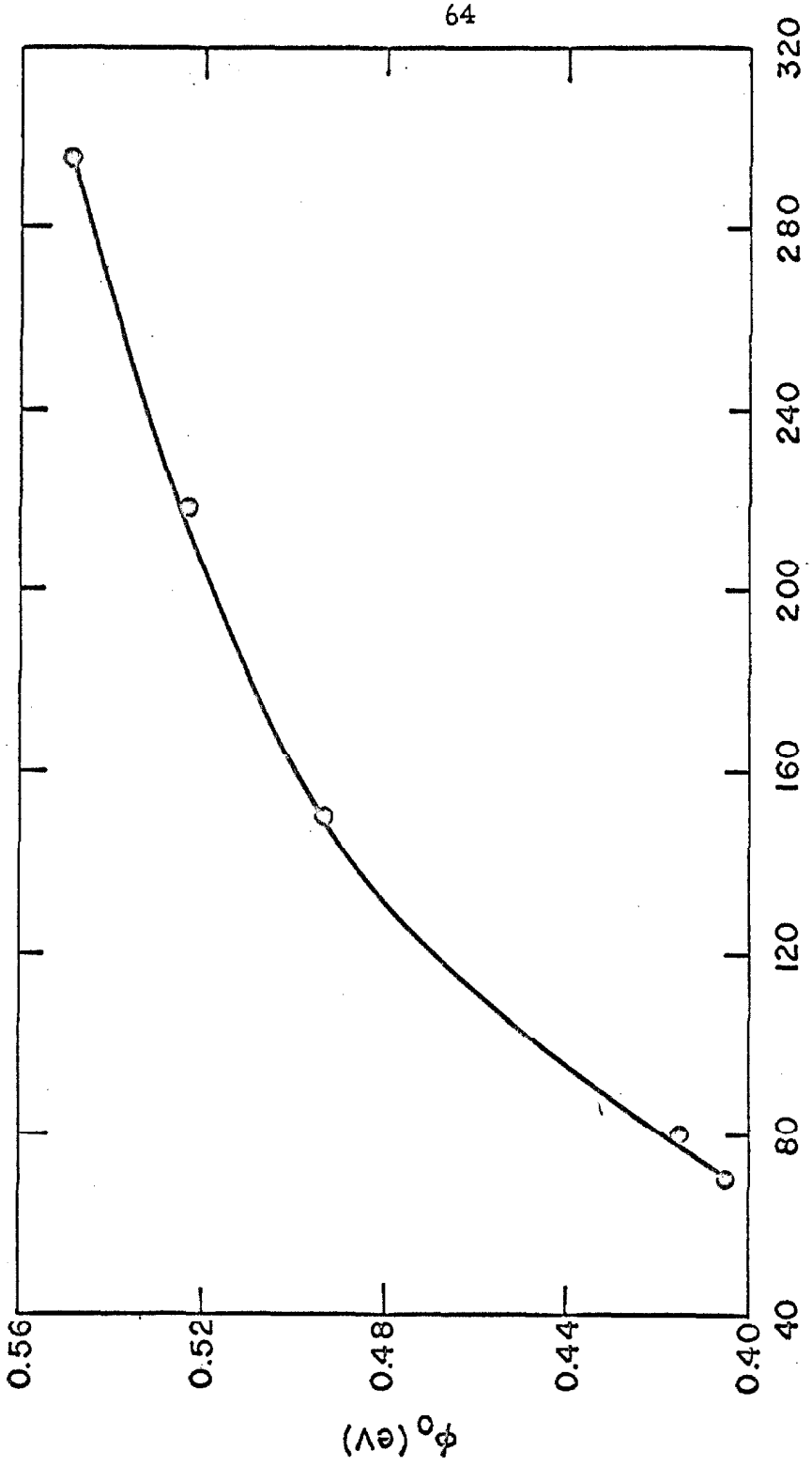

Fig. 21. Activation energy φ_o calculated from 22 and 100°C volt-ampere data assuming φ_o independent of temperature.

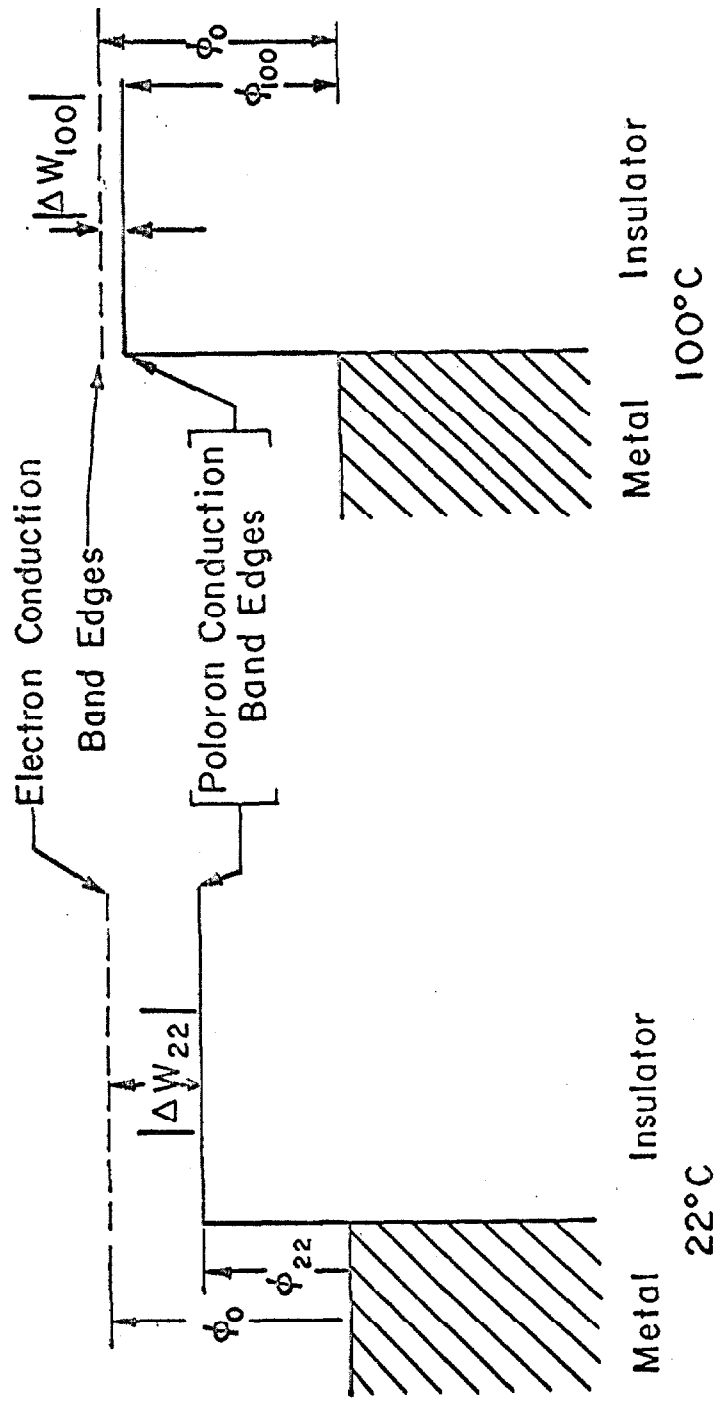

Fig. 22. Illustration of the barrier height dependence on temperature.

$$\varphi_{22} = \varphi_o - |\Delta W_{22}|$$

$$\varphi_{100} = \varphi_o - |\Delta W_{100}|$$

and from equation 84, neglecting the higher order terms which are negligible,

$$|\Delta W_{22}| = \left(\frac{1}{2.5} - \frac{1}{3.28}\right) e_\omega = 0.095 e_\omega$$

$$|\Delta W_{100}| = \left(\frac{1}{2.5} - \frac{1}{2.83}\right) e_\omega = 0.0467\, e_\omega$$

$$= 0.492 |\Delta W_{22}|$$

where

$$e_\omega = e^2 \sqrt{\frac{m^* \omega}{2\hbar}}$$

Then at zero voltage

$$\ln\left(\frac{I_{100}/T_{100}^{2}}{I_{22}/T_{22}^{2}}\right) = \frac{1}{k}\left(\frac{\varphi_{22}}{T_{22}} - \frac{\varphi_{100}}{T_{100}}\right)$$

$$= \frac{T_{100}-T_{22}}{kT_{22}T_{100}}\left[\varphi_o - \frac{T_{100}}{T_{100}-T_{22}}\left(|\Delta W_{22}| - \frac{T_{22}}{T_{100}}|\Delta W_{100}|\right)\right]$$

$$= \frac{T_{100}-T_{22}}{kT_{22}T_{100}}\left(\varphi_o - 2.92\,|\Delta W_{22}|\right)$$

If K were not a function of temperature, the above would be

$$\frac{T_{100} - T_{22}}{kT_{22}T_{100}}\left(\varphi_o - |\Delta W|\right)$$

Taking $2.92\,|\Delta W_{22}| = 0.40$eV, the effective mass ratio becomes 1.53.

Since K is a function of temperature, the resulting temperature dependence of $|\Delta W|$ should be reflected in the curve of $\ln I/T^2$ versus T^{-1}. However, if the polaron model is correct, the polaron effective mass ratio computed from the value of $|\Delta W|$ at any temperature should yield this same value of 1.53. Therefore to test this theory one needs a complete set of Schottky curves over a wide range of temperature in order to obtain the detailed temperature dependence of K, the actual shape of the $\ln I/T^2$ versus T^{-1}

curve, and the corresponding calculation of the effective mass.

Two important restrictions are placed upon injection into a polaron state. First, tunneling into such a state would be truly a second order effect. That is, an electron must actually be in the crystal to form its own potential well. As a result, electrons can only go over the barrier, and the high field conditions of equations 24 and 25 are no longer applicable. Second, not only must the x-directed velocity of the electron be large enough to go over the barrier, but its total velocity while attempting to pass over the barrier must be small enough so that the electron can polarize the ions. This puts a restriction on the total current, since those electrons whose velocities parallel to the interface exceed approximately 10^7 cm/sec cannot be injected into a polaron state. In other words, the polaron current results from electrons that approached the surface in a small cone of velocities whose axis is perpendicular to the surface. Electrons with larger components of velocity parallel to the surface outside this cone cannot be injected into a polaron state. However, these electrons might be injected into the electron conduction band since they experience a smaller dielectric constant which results in a larger Schottky lowering of the barrier due to a larger image force. The question as to which contribution predominates can be found approximately by determining whether $|\Delta W|$ or $\sqrt{e^3 V/d}\ (n^{-1}-K^{-1/2})$

is larger. For the values of $|\Delta W|$, K, and n to be encountered in mica $|\Delta W|$ predominates and the electrons enter the crystal in a polaron state. The question still remains as to why, at these high fields, tunneling into the 0.95eV level does not dominate as depicted in Table II. This will be deferred to the next section on injection at low temperatures.

The samples of ruby muscovite tested lend additional strength to the above model of barrier injection although not at first glance. That is, a higher field was necessary for the same current density even though they have a lower metal-insulator barrier height as discussed in the last section. The lower work function of the ruby muscovite is more than compensated by a smaller Schottky lowering at the barrier due to its higher dielectric constant. Both the Schottky slopes and the data shown in Fig. 27 indicate that at very high frequencies, specifically the 1.5 to 2.0 μ range in Fig. 27, the dielectric constant of ruby muscovite is larger than that of the green by approximately 10% even though their values differ by less than 2% at 50cps.[27]

2.3 Metal-to-Insulator Injection for Thick Films; Temperature Independent Current

For the thicker films at a temperature of 77.4°K the current was found to be more or less independent of temperature in the sense that a 10°K increase in temperature caused less than a

6% increase in current. This suggests the mechanism of current flow in this temperature range is field emission. To investigate this, Fowler-Nordheim plots of the data were made as shown in Figs. 23 and 24. The dashed line shown in Fig. 24 was constructed from the information contained in Fig. 25 wherein the current density was discovered not to be strictly dependent on the field V/d_c but rather a function of $(V + 2)/d_c$.* When F is replaced by $(V + 2)/d_c$ all the curves fall on the dashed line indicated in Fig. 24. Aside from this "bias" two important discrepancies stand out in these curves.

Equation 33 first of all predicts straight lines in Figs. 23 and 24 the slope of which would give an independent value of the barrier height. Even the dotted $F = (V + 2)/dc$ line in F g. 24 has a curvature over its entire length. Secondly, the magnitude of the current density j is lower than theoretically predicted for a $\varphi_o = 0.95eV$ by a factor of approximately 10^9. This reduction in magnitude is not only prevalent in this temperature independent region but also in the temperature dependent region discussed earlier where the factor was approximately 10^7 and also in the case of the 40Å diodes for

---

* Although Fig. 25 has been constructed from aluminum-positive data, the same result is obtained for the opposite polarity; that is, irrespective of the direction of current flow a two volt "bias" aids the process.

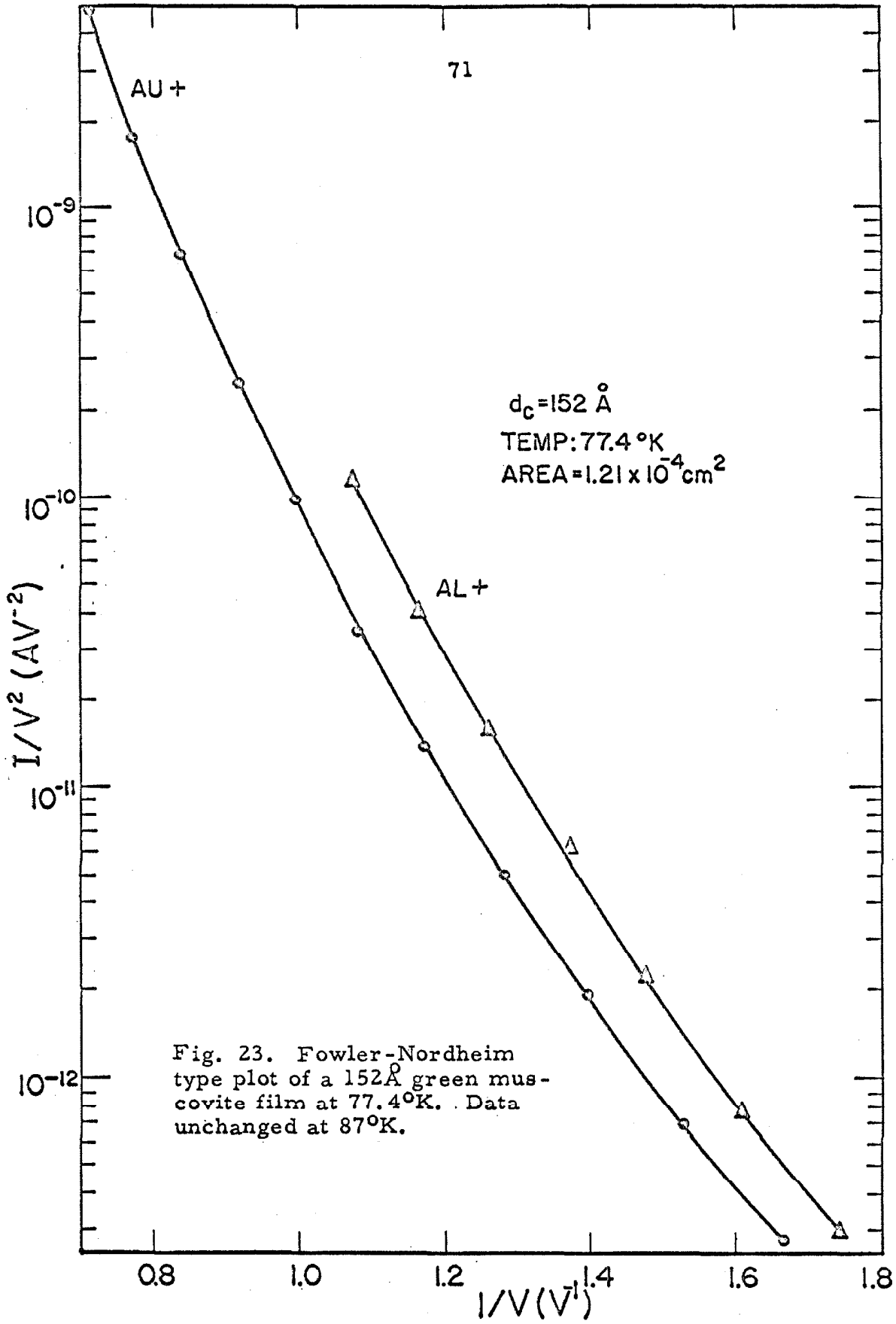

Fig. 23. Fowler-Nordheim type plot of a 152Å green muscovite film at 77.4°K. Data unchanged at 87°K.

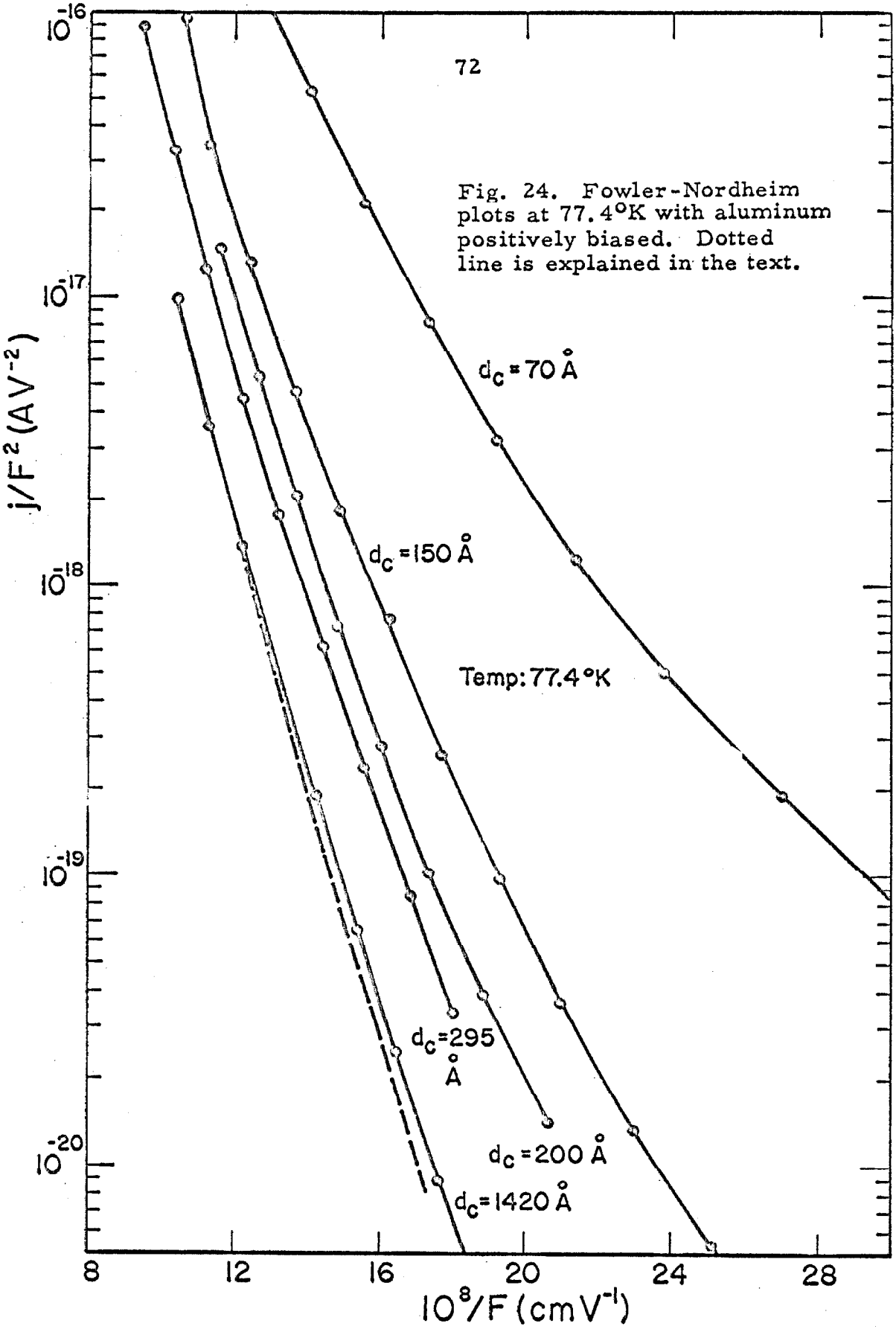

Fig. 24. Fowler-Nordheim plots at 77.4°K with aluminum positively biased. Dotted line is explained in the text.

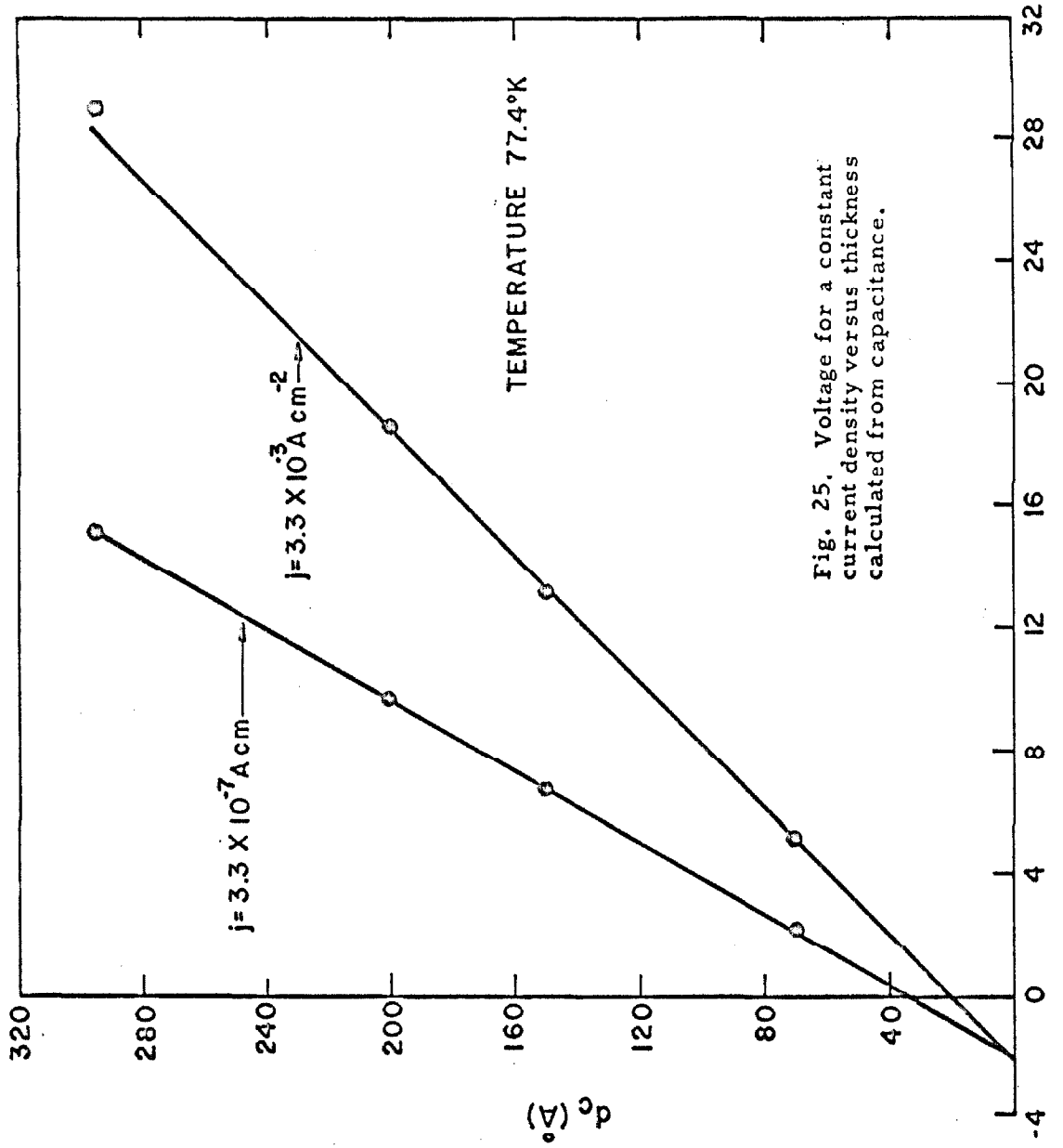

Fig. 25. Voltage for a constant current density versus thickness calculated from capacitance.

voltages greater than 0.95 volts where the factor is about 10^3. Stated briefly metal-to-metal tunneling follows the theory of Chapter I but metal-to-insulator tunneling does not. This situation was hinted at in the discussion of polar crystals in Chapter I. Apparently the insulator's conduction band is quite narrow, and the wave functions applicable are quite localized. Since localized states are nearly orthogonal to incident plane waves in the metal, the crystal presents to these electrons an abrupt discontinuity, and they are for the most part reflected, although they wouldn't be by energy considerations alone. From a theoretical standpo: this problem remains to be solved and considering that a wi' conduction band was assumed in Stratton's tunneling theory, this new outlook puts some doubt into the existence of an electron conduction band at exactly 0.95eV.

2.4 Photoelectric Response

In order to obtain an independent measure of the barrier height, a photoelectric effect experiment was attempted. Unfortunately, the result can only be considered a preliminary one since prior to the vacuum evaporation of the gold the mica was cleaved in air and hence exposed to possible contamination. The experiment consisted of shining chopped monochromatic light onto an extra thin gold film which was negatively biased with respect to the aluminum. The resulting photoelectric current was then synchronously detected.

Shown in Fig. 26 is a plot of the photocurrent through the diode per incident photon flux versus incident photon energy $h\nu$. The intercept on the photon energy axis at 0.8eV indicates that this would be the value of the photoelectric barrier height if the effect of air contamination were unimportant. If it is unimportant then it is the author's judgment that the photoelectric barrier height is the actual one and the tunneling value of 0.95eV is in error due to an untrue energy-momentum relation in the forbidden band which was used in equation 22. If this is the case the separation between the band edges of the polaron and electronic conduction bands is only 0.25eV, from which $2.92|\Delta W_{22}| =$ 0.25eV, and which in turn means the effective mass ratio at the bottom of the polaron conduction band is 0.60.

2.5 Other Observations and Possible Mechanisms

The Frenkel effect discussed in Chapter I depends on the existence of traps in the insulator. Figure 27 shows the optical absorption data taken on samples of green and ruby mica. The absorption maximum at 2.72μ has been verified in the literature as being an OH reststrahlen band,[23, 25] and most likely the dips at 2.40μ and 2.15μ are combination bands of this and other resonances. However, even under the extreme assumption that the traps in muscovite are masked out by these vibration spectra, an upper limit can be found for their concentration. The maximum in the absorption coefficient, μ_{max}, is related to the number of traps

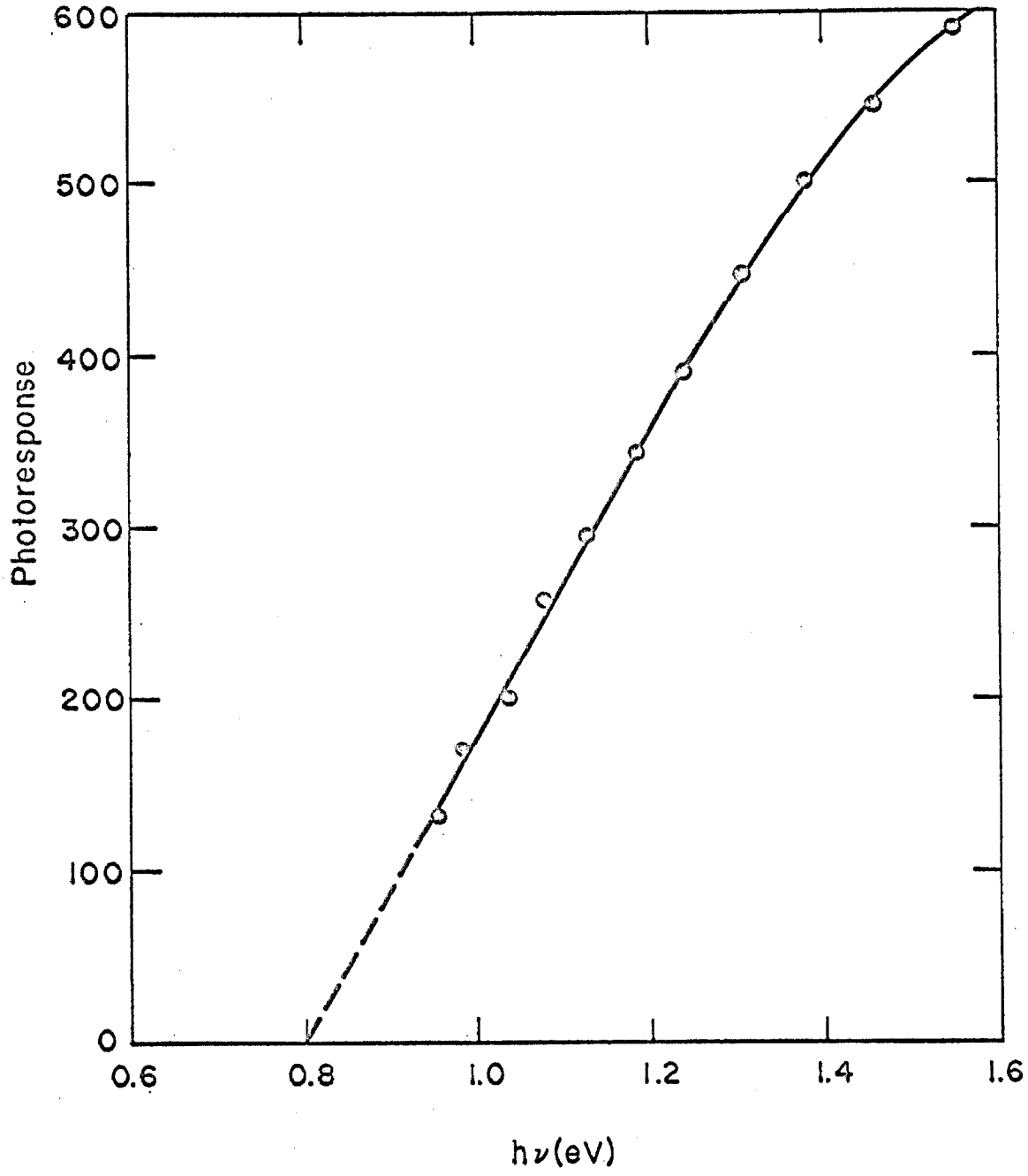

Fig. 26. Photocurrent per incident photon flux (arbitrary units) versus incident photon energy.

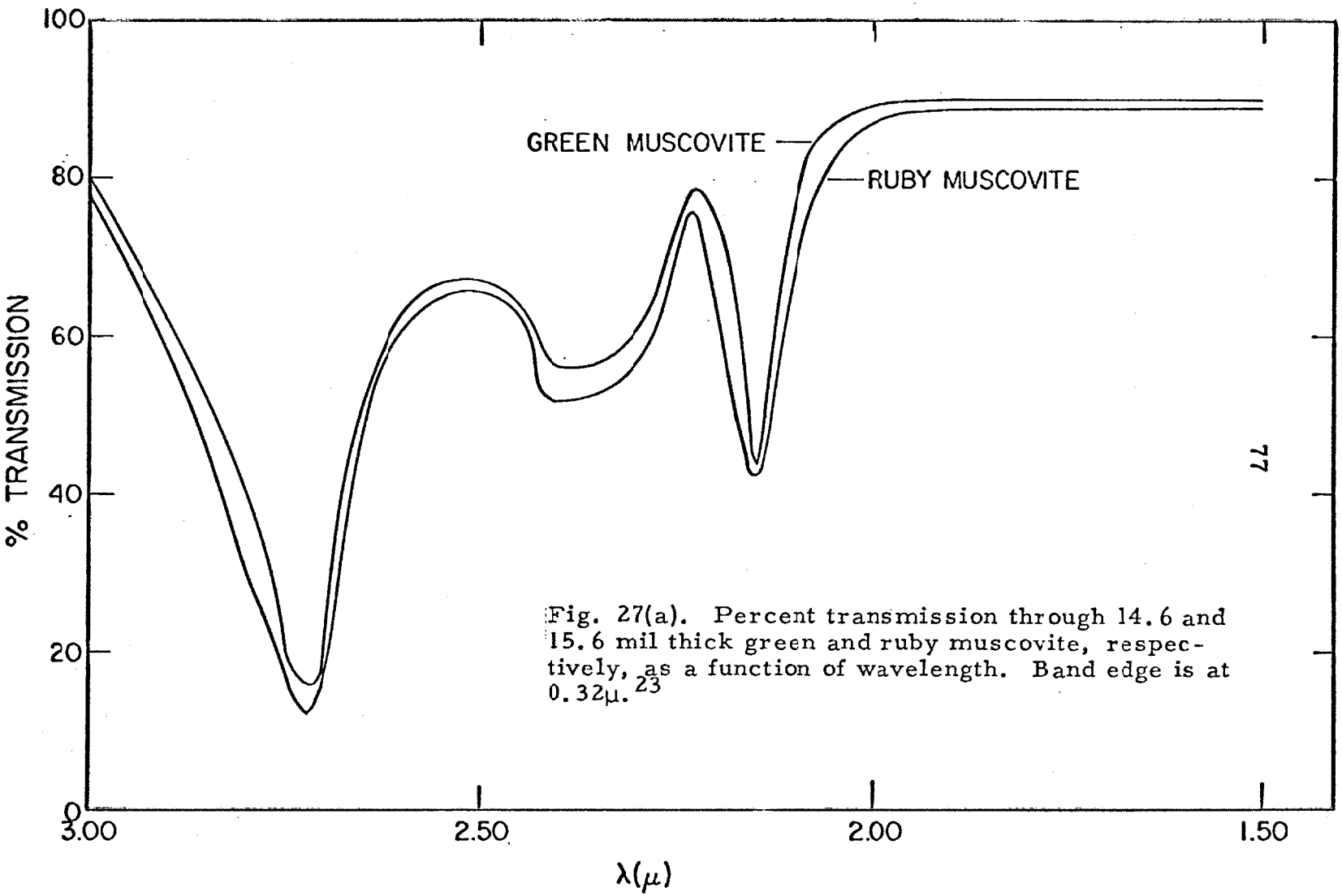

Fig. 27(a). Percent transmission through 14.6 and 15.6 mil thick green and ruby muscovite, respectively, as a function of wavelength. Band edge is at 0.32μ.[23]

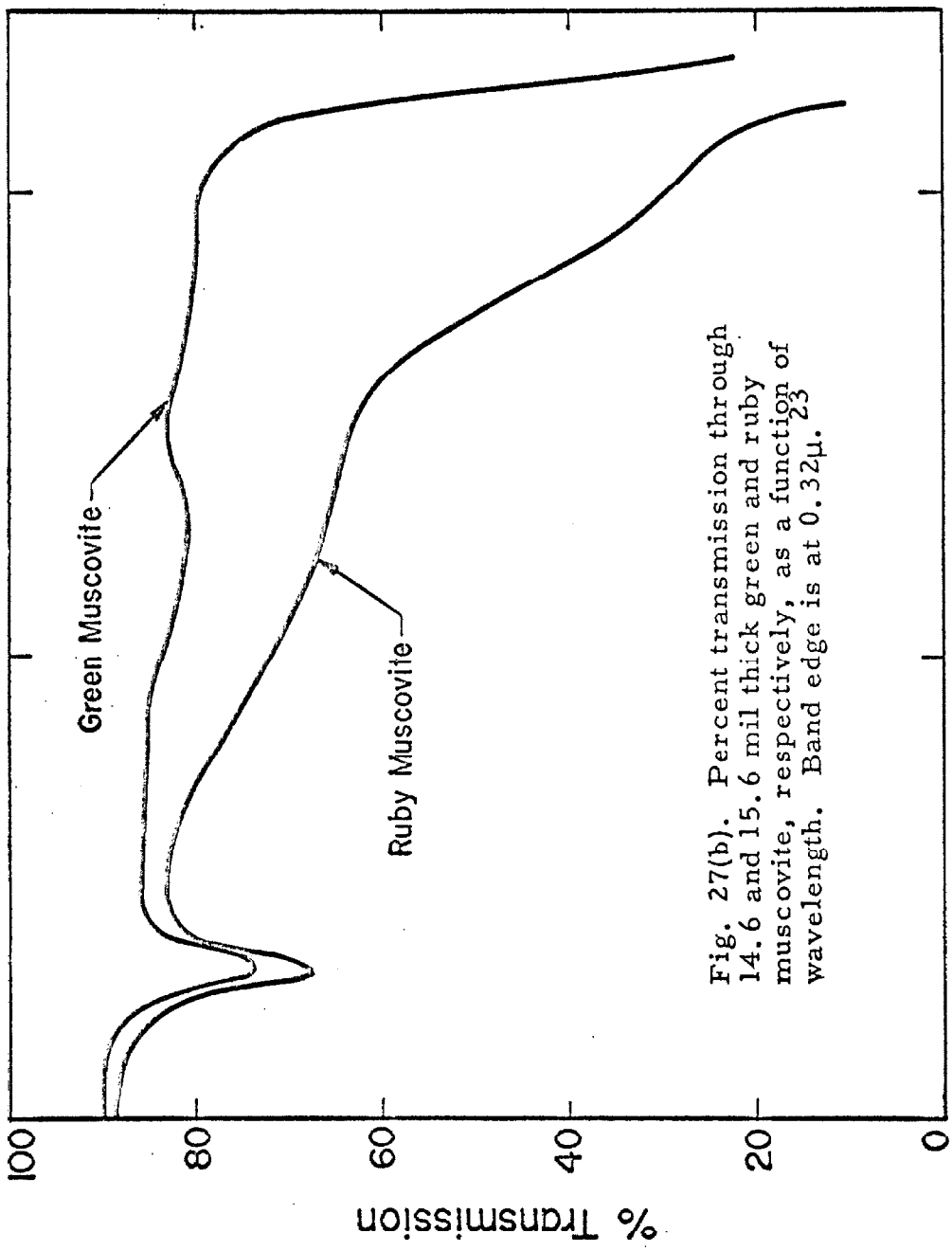

Fig. 27(b). Percent transmission through 14.6 and 15.6 mil thick green and ruby muscovite, respectively, as a function of wavelength. Band edge is at 0.32μ.[23]

per cm^3, N, by[28]

$$Nf \approx 10^{17} \frac{n}{(n^2 + 2)^2} \mu_{max} U \qquad (113)$$

where n is the refractive index, U the width of the absorption curve at half-maximum, and f is the oscillator strength, typically of the order of 0.5. At 2.72μ, $\mu_{max} = 57.1 cm^{-1}$, $U = 1.1 \times 10^{-5} cm$, n = 1.58 and for f = 0.5,

$$N < 10^{13} \ cm^{-3}$$

or less than 1000 traps within the diode area for a 100Å thick film. Such a small number would have difficulty in supporting a current of 10^{-7} amps. On the other hand, if the traps were present but for the most part empty because of the presence of acceptors and thus do not show up in the absorption data, the temperature dependence of the conductivity would be by equation 112

$$\sigma = \sigma_o \exp \left[2 \left(\frac{e^3 F}{K} \right)^{1/2} / kT \right]$$

as discussed in Chapter I. Therefore, for the Frenkel effect to be the correct explanation of the experimental results

$$K = 4(3.28) = 13.1$$

which is impossible as this value is above the value at 50cps of 8.[27]

Space-charge-limited current is ruled out as a possibility because of the linear relation between the voltage required for a constant current density and the thickness.[29] Furthermore, no dependence of the capacitance upon frequency in the range of 1000 to 100,000 cps or a bias of up to 5×10^6 volts/cm as is generally observed,[30] was seen. In addition a 10μsec long voltage pulse indicated no initial surge in current, at least not beyond the natural 8μsec charging time of the diode's capacitance.

The effect of geometry alone on the diode's characteristic proved to be unimportant since the volt-ampere data on an aluminum-mica-aluminum structure was symmetrical.

The possibility of a diffusion of aluminum into the mica during the 200°C anneal (see Appendix I) having an effect on the results is ruled out because a 400°C anneal for 2 hours produced no change.

The non-zero intercept of the plot of the voltage necessary for a constant current density versus thickness computed from capacitance measurements was first erroneously thought to be an indication of field penetration into the metal.[31] That is, it was thought that only capacitance measurements would be sensitive to the penetration, i.e.,

$$\frac{1}{C} = \frac{d_c}{\epsilon_o K A} \tag{114}$$

for

$$d_c = d + \frac{K}{K_m}\,\delta \qquad (115)$$

where d is the actual thickness of the insulator, δ is the sum total of the effective penetration distances into both metals, and K and K_m are the dielectric constants of the insulator and metal, respectively; whereas the field across the insulator would be strictly V/d. The latter is not the case, however, as the field across the insulator would be V/d_c. Therefore, a plot of d_c (or C^{-1} as in reference 31) versus V for a constant current density would be a straight line through the origin and hence have no non-zero intercept. Even though the intercept method is not satisfactory for the investigation of field penetration into a metal, the concept of field penetration is still an interesting one and should be observable from two other standpoints. First the fact that mica can only be cleaved in 10Å increments[4] allows one a direct measure of $K\delta/K_m$ from capacitance measurements and equations 114 and 115.* Applying this

---

* This method presupposes an accurate knowledge of K at the signal frequency (100kc) of the capacitance bridge. The value of K of 7.6 that was used was experimentally determined from the capacitance of several bulk sheets of mica that were aluminized on both sides and whose thicknesses could be measured directly with a micrometer.

technique to the 30Å films it was possible to place an upper limit on $K\delta/K_m$ of 3Å, this figure being the result of a $\pm$ 10% accuracy in measuring the very small areas of the gold dots. This value is not nearly as large as the 25 Å reported by Meyerhofer and Ochs,[22] who inferred their value from tunneling data taken on BeO and Al_2O_3 thin films. Secondly, field penetration could be expected to lower the entire band structure of the metal near the surface and thus make φ a function of field, or

$$\varphi(V) \approx \varphi(o) - \frac{K}{K_m} \delta \frac{V}{d_c} \qquad (116)$$

as shown in Fig. 28. This would introduce an upward concaveness to the ln I versus $\sqrt{V}$ curves, and their excellent linearity can also establish an upper limit of

$$\frac{K}{K_m} \delta < 0.1\text{Å}$$

since the currents at the largest fields were at least within 20% of the straight Schottky line.

The change in the characteristics of the 30 and 40Å films with time has already been mentioned. For the most part their tunnel resistances, R, drifted downwards by as much as a factor of two in six months. Some did increase slightly. The reproducibility of R on the same sample was within $\pm$10% and within $\pm$25% from sample to sample. Similar variations from sample to sample on the thicker

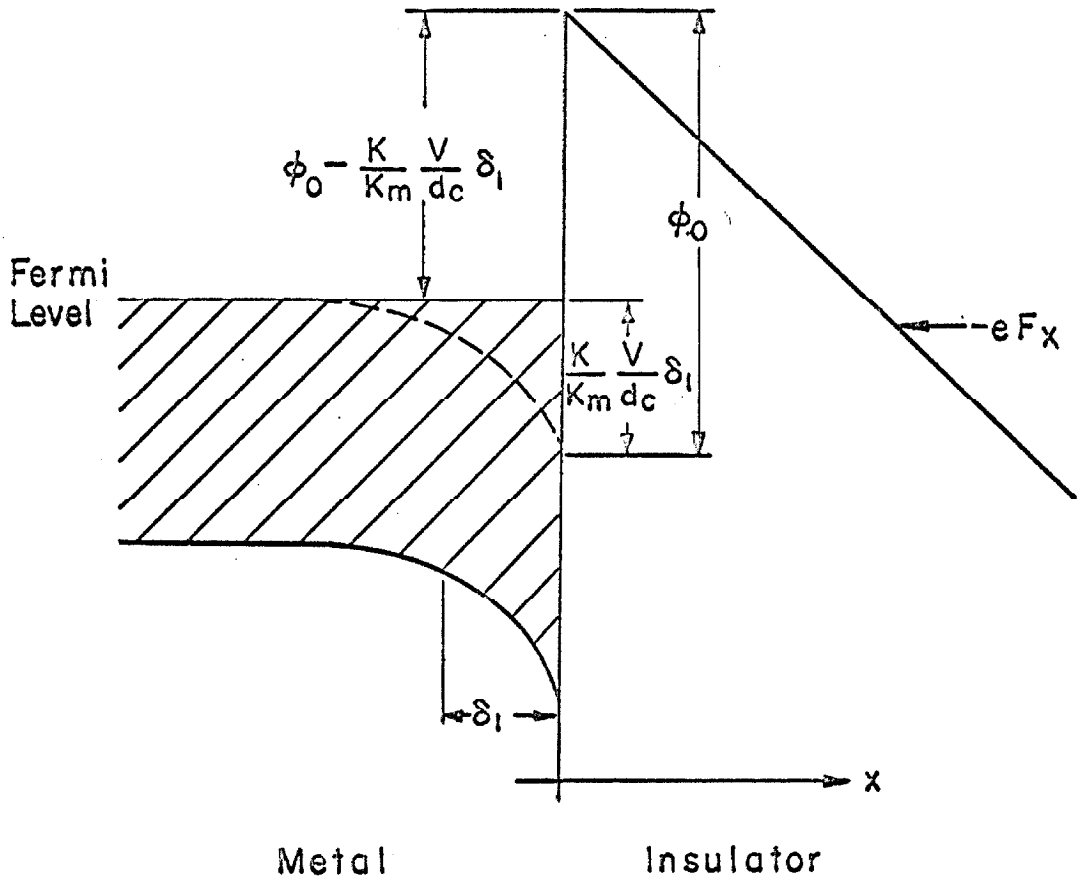

Fig. 28. Illustrating the effect of field penetration on the barrier height, neglecting image forces.

diodes did not occur and might have been masked out because of the exponential dependence of current on voltage.

CHAPTER III

CONCLUSIONS

Tunneling theory provides a self-consistent quantitative description to explain the metal-to-metal tunneling across the mica but was completely inadequate in both magnitude and functional dependence for voltages much larger than the barrier height, where injection is into the conduction band of the insulator itself. This apparent inconsistency would be resolved if the correct wave function for the electron in the conduction band of muscovite were of the localized or tight binding variety. That is, the WKB approximation used in the derivation is a plane wave type of solution and could only be correctly applied to the loose binding situation in metals.

Furthermore, tunneling into this narrow tight-binding band is depressed to such a degree that at room temperature injection into polaron states, whose conduction band is necessarily lower, would explain the anomalous temperature dependence and if correct would predict a temperature dependent barrier height.

These experiments also show that, although the tunneling theory gives a value of φ_o consistent with the results of two different thicknesses, the preliminary photoresponse data suggest that this is larger than the actual distance to the bottom of the conduction band.

Finally, an upper limit to the anomalous capacitance, considerably smaller than previously thought, is suggested by the extreme linearity of the Schottky slopes.

APPENDIX I

FABRICATION AND MEASUREMENT TECHNIQUES

A. Fabrication

The technique for making these diodes was developed by Foote and Kazan[8] and consists essentially of evaporating a metal on one side of a sheet of mica, attaching this side to a flat surface and then stripping the remainder of the sheet off leaving only a thin film of mica on the surface. A matrix of metal dots are then evaporated making a large number of diodes on each sample. This procedure was modified only in that the cleaving was done inside the vacuum chamber in such a manner that the surface of the mica was never exposed to the atmosphere. Details of the procedure are as follows:

1. Freshly cleave mica on both sides leaving it scratch free and approximately 0.001 inch thick. The mica was supplied by Mica Products Company of Los Angeles and consisted of clear green and ruby muscovite of Grades NMF and NMC.
2. This mica sheet is then bonded between two glass microscope slides as shown in Fig. 29, the top slide having been cut down to a 3/4 inch square. The top 1/8 inch aluminum block has been drilled and tapped. Torr-Seal (made by Varian Associates of Palo Alto, California) was the epoxy

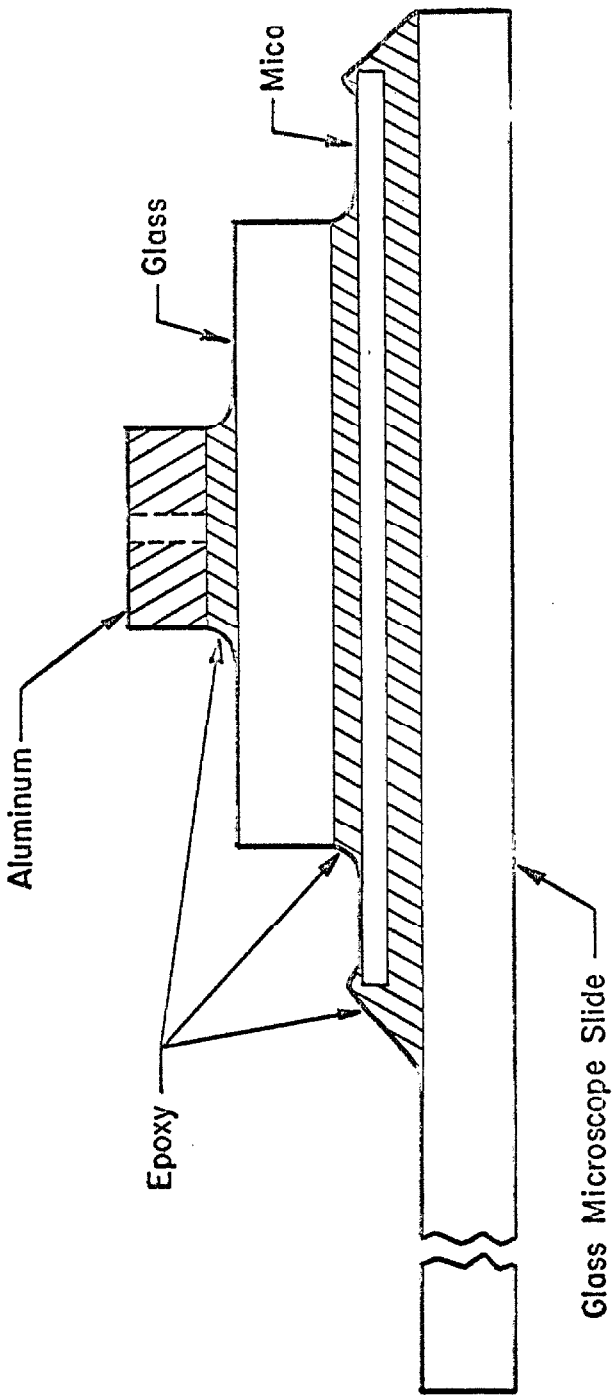

Fig. 29. Preparation for the first cleave.

used for the bonding.

3. This glass-mica-glass sandwich is then mounted in the vacuum system as shown in Fig. 30. The bottom slide is clamped down and the top slide attached to the arm. Cleavage can now be done at a high vacuum (10^{-6} Torr) by applying a torque to the arm by means of magnets as shown and aluminum evaporated on the bottom sheet. The vacuum system used was a 2 inch oil diffusion system with a Zeolite trap designed to prevent oil-creep.

4. Anneal the aluminum in air at 200°C for 2 hours. An attempt to avoid this step resulted in the gold dots bubbling up and falling off over a period of 24 to 48 hours.

5. Indium solder copper leads to the aluminum surface and epoxy on the blocks as shown in Fig. 31.

6. Cleave as in (3) and rotate the arm over to a mask which in this case was composed of 5 x 5 mil holes spaced 10 mils apart and evaporate the second electrode.

Usually the sample will consist of patches of different thicknesses ranging typically from 100Å or less up to several microns. If not thin enough, recleave. The one requirement on the first metal is that its adhesion to the mica be stronger than the force required for cleavage. Aluminum is satisfactory, chromium and cobalt unsatisfactory.[8]

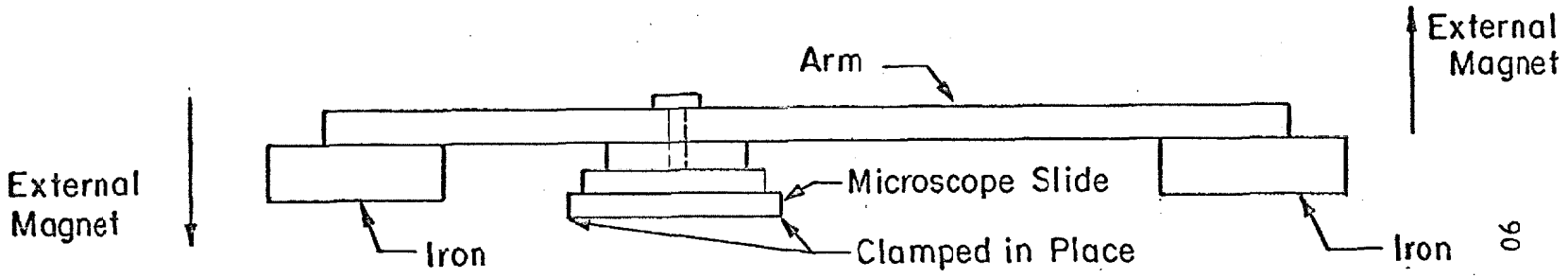

Fig. 30. Setup for cleaving in the vacuum chamber.

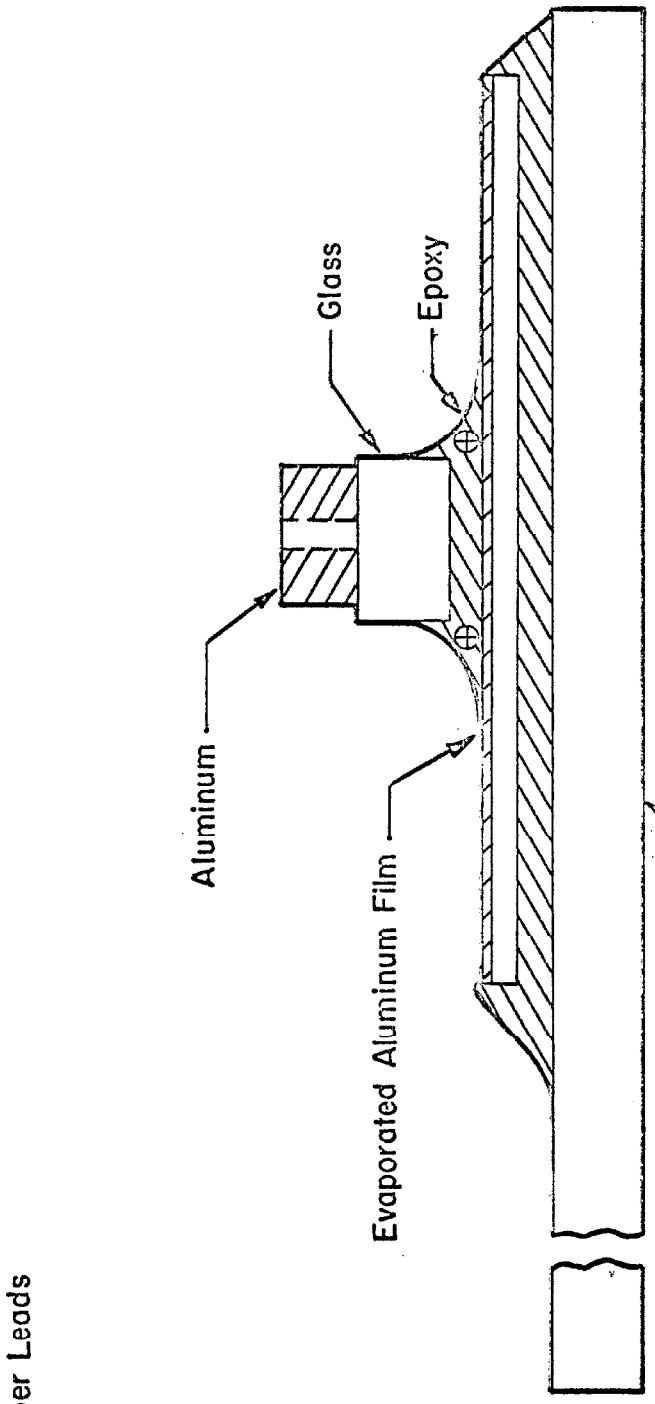

Fig. 31. Preparation for the second cleave.

B. Measurement Techniques

Thickness measurements were calculated from the diode's capacitance and area. That is

$$d_c = \frac{\varepsilon_o K A}{C}$$

wherein a K of 7.6 was used, a value calculated in turn from the capacitance, thickness, and area of several bulk sheets of mica which were aluminized on both sides and whose thicknesses could be measured directly with a micrometer to three significant figures. Capacitance was measured using a Boonton Electronics Corporation Capacitance Bridge Model 74C-S8, whose signal frequency was 100 kc and which had the added capability that allowed one to apply an adjustable dc bias across the diode while measuring its capacitance.

Currents were measured using both the Hewlett Packard Model 425A microvolt-ammeter and the Cary Electrometer Model 31 made by Applied Physics Corporation. No diode was given any consideration unless it was completely surrounded by dots of identical characteristics.

Measurements at 100°C were performed in a cryoflask made by Texas Instruments, Model No. CLF 1/2, in which the sample is in a vacuum chamber but in thermal contact through a copper plate to a slowly boiling bath of water. The dewar was fitted with a

micro-positioner so as to make contact to more than one dot while at this temperature. Measurements at 77 and 87°K were more conveniently taken directly in baths of liquid nitrogen and argon, respectively.

All optical data was taken with the use of a Gaertner prism monochrometer Model L119 using tungsten and Xenon light sources where applicable. A thermocouple made by Charles M. Reeder Company of Detroit was used to obtain the transmittance data of Fig. 28. The photoelectric response data was taken with the light incident on an extra thin (~200Å) gold film negatively biased and the pickup current synchronously detected to the 50cps chopped light source.

REFERENCES

1. C. A. Mead, Proc. Inst. Radio Engrs. 48, 359 (1960); 48, 1478 (1960); C. A. Mead, J. Appl. Phys. 32, 646 (1961); J. Cohen, J. Appl. Phys. 33, 1999 (1962); Appl. Phys. Letters 3, 61 (1962); H. Kanter and W. A. Feibelman, J. Appl. Phys. 33, 3580 (1962).
2. I. Giaever and K. Megerle, Phys. Rev. 122, 1101 (1961); P. W. Anderson and J. M. Rowell, Phys. Rev. Letters 10, 230 (1963).
3. T. E. Hartman and J. S. Chivian (to be published).
4. W. Hückel, Ahorganische Strukturchemie (Ferdinand Enke, Stuttgart, Germany, 1948), p. 742; F. H. Norton, Elements of Ceramics (Addison-Wesley Press, Inc., Cambridge, 1952), p. 12.
5. A. Von Hippel, Phys. Rev. 54, 1096 (1938).
6. A. V. Mal'tsev, Fiz . Dielecktritov (Moscow: Akad. Nauk S.S.S.R.) Sbovnik 1958, 63; see Chemical Abstracts 55, 13988f (1961).
7. Y. Frenkel, Tech. Phys. U.S.S.R. 5, 685 (1938) (in English); C. A. Mead, Phys. Rev. 128, 2088 (1962).
8. D. P. Foote and B. Kazan, ASD-TDR-63-640.

9. R. Stratton, J. Phys. Chem. Solids 23, 1177 (1962).

10. E. L. Murphy and R. H. Good, Jr. Phys. Rev. 102, 1464 (1956).

11. R. Fowler and L. Nordheim, Proc. Roy. Soc. (London) A119, 173 (1928); L. Nordheim, ibid A121, 626 (1928).

12. W A. Harrison, Phys. Rev. 123, 85 (1961); see also P. J. Price and J. M. Radcliffe, IBM J. Research Develop 3, 364 (1959).

13. A. Sommerfeld and H. Bethe, Handbuch der Physik (Edited by H. Geiger and K. Scheel, Springer, Berlin, 1933), vol. XXIV/2, p. 450.

14. E. Jahnke and F. Emde, Tables of Functions (Dover Publications, New York, 1945), p. 16.

15. H. Fröhlich, Polarons and Excitons (Edited by C. G. Kuper and G. D. Whitfield, Plenum Press, New York, 1963).

16. G. R. Allcock, Advances in Physics 5, 412 (1956) see Table I, p. 450 for a resumé of the subject.

17. M. Sachs, Solid State Theory (McGraw-Hill, New York, 1963), p. 72.

18. R. A. Smith, Wave Mechanics of Crystalline Solids (Chapman and Hall, London, 1961), p. 149.

19. C. Kittel, Introduction to Solid State Physics (John Wiley and Sons, Inc., New York, 1956), 2nd ed., p. 358.

20. E. Spenke, Electronic Semiconductors (McGraw-Hill, New York, 1958).

21. T. E. Hartman, private communication.

22. D. Meyerhofer and S. A. Ochs, J. Appl. Phys. 34, 2535 (1963).

23. S. Ruthberg, M. W. Barnes and R. H. Noyce, J. Research Natl. Bur. Standards 67A, 309 (1963).

24. R. Braunstein and E. O. Kane, J. Phys. Chem. Solids 23, 1423 (1962).

25. T. E. Hartman, J. Appl. Phys. 33, 3427 (1962).

26. F. Matossi and O. Bronder, Z. Physik 111, 1 (1938).

27. S. Mandal and R. N. Dhar, Central Glass and Ceram. Research Inst. Bull. (India) 7, 161 (1960).

28. D. L. Dexter, Solid State Electronics (Edited by F. Seitz and D. Turnbull, Academic Press, Inc., New York and London, 1958), Vol. 6.

29. A. Rose, Phys. Rev. 97, 1538 (1955); M. A. Lampert, Phys. Rev. 103, 1648 (1956).

30. R. S. Muller, "Electronic Processes in Au-CdS-In Diodes", Calif. Inst. of Technology, Solid State Electronics Laboratories Report, 1962.

31. C. A. Mead, Phys. Rev. Letters 6, 545 (1961).